

Alkali-activated refractory wastes exposed to high temperatures: development and characterization

*Original*

Alkali-activated refractory wastes exposed to high temperatures: development and characterization / Coppola, B.; Tardivat, C.; Richaud, S.; Tulliani, J. M.; Montanaro, L.; Palmero, P.. - In: JOURNAL OF THE EUROPEAN CERAMIC SOCIETY. - ISSN 0955-2219. - STAMPA. - 40:8(2020), pp. 3314-3326. [10.1016/j.jeurceramsoc.2020.02.052]

*Availability:*

This version is available at: 11583/2816432 since: 2020-04-29T13:22:32Z

*Publisher:*

Elsevier Ltd

*Published*

DOI:10.1016/j.jeurceramsoc.2020.02.052

*Terms of use:*

This article is made available under terms and conditions as specified in the corresponding bibliographic description in the repository

*Publisher copyright*

Elsevier postprint/Author's Accepted Manuscript

© 2020. This manuscript version is made available under the CC-BY-NC-ND 4.0 license  
<http://creativecommons.org/licenses/by-nc-nd/4.0/>. The final authenticated version is available online at:  
<http://dx.doi.org/10.1016/j.jeurceramsoc.2020.02.052>

(Article begins on next page)

# **Alkali-activated refractory wastes exposed to high temperatures: development and characterization**

Bartolomeo Coppola<sup>a,\*</sup>, Caroline Tardivat<sup>b</sup>, Stéphane Richaud<sup>b</sup>, Jean-Marc Tulliani<sup>a</sup>, Laura Montanaro<sup>a</sup>, Paola Palmero<sup>a</sup>

<sup>a</sup>Politecnico di Torino, Department of Applied Science and Technology, INSTM R.U. Lince Laboratory, Corso Duca Degli Abruzzi, 24, Italy

<sup>b</sup>LSFC Laboratoire de Synthèse et Fonctionnalisation des céramiques UMR 3080 CNRS / Saint-Gobain CREE, Saint-Gobain Research Provence, 550 avenue Alphonse Jauffret, Cavaillon, France

\*Corresponding author: bartolomeo.coppola@polito.it

## **Abstract**

The feasibility to prepare alkali-activated materials starting from refractory wastes and their properties after exposure to high temperatures (800, 1000, 1200 and 1400 °C) were investigated. Two different aluminosilicate wastes were used: chamotte (CH, mainly composed of corundum, mullite and andalusite) and alumina-zirconia-silica (AZS, composed by baddeleyite, corundum and amorphous silica). Very high mechanical properties were achieved in both cases (28-days compressive strength of approx. 70 and 60 MPa for CH- and AZS-based pastes, respectively). Then, alkali-activated pastes were exposed to high temperatures. For both kinds of samples, a sharp increase of mechanical properties was obtained after exposure to 800 and 1000 °C thanks to the matrix densification. Above 1000 °C viscous sintering occurs leading to a further increase of mechanical properties. AZS-based materials were able to withstand high temperatures up to 1400 °C while CH-based pastes mechanical properties decrease at 1400 °C due to andalusite decomposition.

## **Keywords**

Chamotte; AZS; Alkali-activation; Refractory; High-temperature.

## 1. Introduction

Nowadays, alkali-activated materials are receiving increasing attention, due to their attractive physical and mechanical properties (e.g., short setting time, high mechanical strength, high-temperature resistance, low sensitivity to chemical attack etc.), and lower environmental impact as respect to traditional construction materials [1-3], mainly due to their room- or low-temperature processing. Most important, it is possible to integrate different types of industrial waste into their manufacturing [4], limiting waste landfilling and moving towards an effective circular economy approach.

When preparing alkali-activated materials, typical feedstock powders are amorphous or semi-crystalline aluminosilicates like metakaolin, granulated blast furnace slag and fly ashes [1-3], whose poorly-organized structure accounts for their high reactivity under alkaline conditions. Recently, the possibility to exploit highly crystalline powders has been investigated as well, with the aim of further extending the range of available waste to be used in the geopolymer process. In some of our previous researches, in fact, we investigated the use of semi-crystalline and of well-crystallized mineral waste powders (such as marble sludge, stone muds and construction and demolition wastes (CDW)) as precursors for alkali-activated materials [5-7]. However, a more general approach implies the use of such mineral particles as filler in a geopolymer matrix, providing composites for a range of applications. For instance, refractory particles and fibers have been exploited in geopolymers in order to improve fire resistance [8-10], thermal insulation [11-13], to produce refractories for the glass industry [14] and for other applications requiring good performance at high temperatures [15].

Refractories are ceramic materials specifically designed for high-temperatures applications, produced in large quantities to meet a real demand in three major industrial fields: *i*) traditional high-temperature sector (glass furnaces, steelmaking, nonferrous metallurgy, cement kiln, petrochemicals, etc.); *ii*) treatment and energy recovery from waste (domestic waste incineration, waste vitrification); *iii*) refractory linings for the energy sectors (production of biofuels, heat and electricity) [16]. Such industrial demand accounts for the very high worldwide refractory production (approx. 35-40 million tons per year [17]) leading, consequently, to a very huge amount of waste (approx. 28 million tons per year [17]). Alumina, silica, magnesia, zirconia and their composites are the typical raw materials to fabricate refractories [18,19]. In particular way,

aluminosilicates are the oldest and most widely used refractories in the world, being their properties mainly governed by the mullite content [20]. In fact, they are composed by corundum ( $\text{Al}_2\text{O}_3$ ),  $\text{Al}_2\text{SiO}_5$  polymorphisms (andalusite, sillimanite and kyanite) and mullite ( $\text{Al}_6\text{Si}_2\text{O}_{13}$ ), with small amounts of glassy phase between grain boundaries [20]. Another important group of refractories are those containing zirconia, alumina and silica (AZS) prepared via electrofusion-casting. The addition of zirconia (between 30 and 42 wt%) to aluminosilicate refractories was introduced at the beginning of the last century, to improve the corrosion resistance in glass furnaces [21,22]. A characteristic of the electro-melted refractories is their minimum porosity (1–2%), being this feature of great importance as it minimizes the glass-refractory interface [21-24].

As a smart strategy to reuse refractory wastes, their use as aggregates or fillers in geopolymers has been already investigated [25-36], as stated before. The addition of these fillers further improves the high – temperature resistance and contrasts the shrinkage [27,29,31,34,36]. Numerous studies have already demonstrated the better high temperature behavior of geopolymers compared to cementitious materials [37,38]. In fact, at temperatures higher than  $1000^\circ\text{C}$ , the compressive strength of Portland cement can be reduced as much as 90% [37], due to dehydration of hydrated compounds, degradation of the calcium silicate hydrates (C-S-H) and generation of internal thermal stress gradients. On the opposite, geopolymer concretes, consisting of non-hydrated aluminosilicate gel binding phases, not containing large amounts of chemi- or physi-sorbed water when compared with C-S-H gels, and characterized by an open pore structure, are able to withstand temperatures in the range of  $600\text{--}800^\circ\text{C}$  with minor loss of strength [37]. The addition of refractory particles further improves such behavior, reducing cracks, improving dimensional stability and providing pathways for gentle dehydration. Even if the mostly used fillers are in granular forms (e.g, silica, calcite and dolime (softly burnt dolomite) sand [39-40], ground porcelain and high-alumina refractory brick [41,42],  $\alpha\text{-Al}_2\text{O}_3$ , chamotte and cordierite powder [28,30,26]), some tests with fiber reinforcement – in analogy to cement technology [44,45] – were performed as well (e.g., SiC fibers [46], basalt fibers [47]).

Besides their role as a filler, and according to their aluminosilicate composition, fine refractory waste can be potentially used as precursors for new alkaline-activated materials. Therefore, as a point of innovation compared to previous literature, aim of this research is to investigate the behavior of fine refractory particles

under alkaline-activation conditions. To this purpose, two different types of refractory waste were investigated: a chamotte and an AZS powder. Besides their aluminosilicate nature, the presence of a siliceous glassy phase (in particular in the case of AZS samples) could be positively exploited in the alkaline activation process. Once proved the feasibility to develop alkali-activated pastes starting from these wastes, their high-temperature behavior (from 800 °C to 1400 °C) was investigated in order to ascertain possible high-temperature applications. Therefore, the hardened samples have been submitted to several characterizations, to investigate and their physical-mechanical behavior, as well as their microstructural and compositional evolution in that temperature range.

## 2. Experimental

### 2.1 Materials

Two different materials were used in this study, they were chosen to be representative of a typical waste obtained from the recycling of used refractory materials: chamotte (CH) and alumina-zirconia-silica (AZS) powders, both provided by Saint-Gobain Research Provence (Cavaillon, France). AZS ( $\rho = 3.75 \text{ g/cm}^3$ ) is a typical refractory used in glass furnaces, obtained by electrofusion. CH ( $\rho = 3.00 \text{ g/cm}^3$ ) is a refractory material mainly composed of alumina and silica, obtained by shaping and sintering. Both samples were provided as ground powders, and were sieved under 40  $\mu\text{m}$ .

X-ray diffraction (XRD) patterns of the two powders are reported in Figure 1. Chamotte contains mainly andalusite ( $\text{Al}_2\text{SiO}_5$ , JCPDS file n°00-039-0376), mullite ( $\text{Al}_6\text{O}_{13}\text{Si}_2$ , JCPDS file n°00-015-0776) and corundum ( $\alpha\text{-Al}_2\text{O}_3$ , JCPDS file n°00-042-1468), while quartz ( $\text{SiO}_2$ , JCPDS file n°00-012-0708), cristobalite ( $\text{SiO}_2$ , JCPDS file n°00-039-1425), albite ( $\text{AlNaO}_8\text{Si}_3$  JCPDS file n°00-009-0466) and anorthite ( $\text{Al}_2\text{CaO}_8\text{Si}_2$  JCPDS file n°00-041-1486) are present as traces (Figure 1a). On the other side, the XRD pattern of AZS (Figure 1b) is less complex and presents mainly corundum and monoclinic  $\text{ZrO}_2$  (baddeleyite, JCPDS file n°00-037-1484) and some traces of tetragonal zirconia (JCPDS file n°00-050-1089).

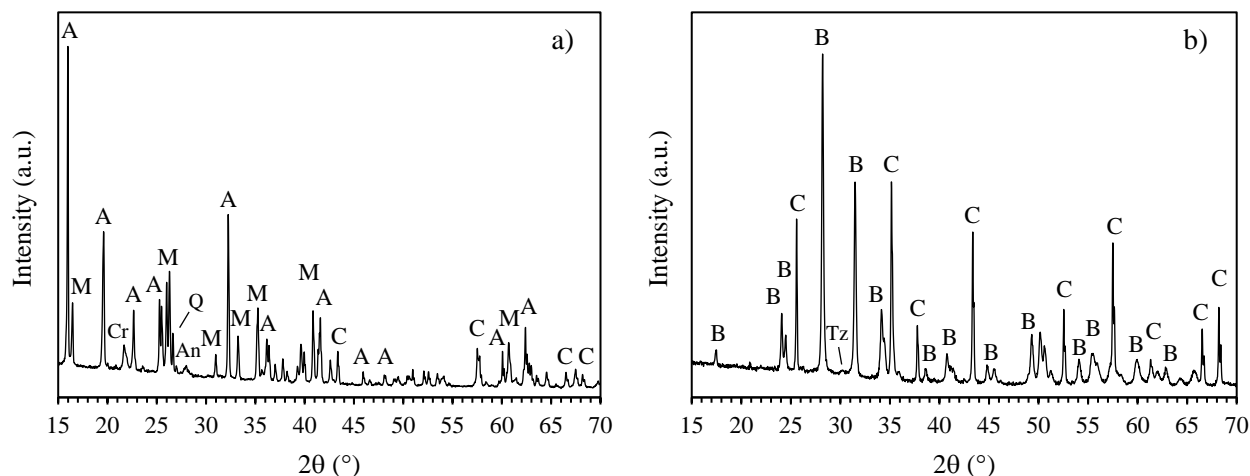


**Figure 1:** XRD patterns of as-received a) CH and b) AZS powders (A = Andalusite, An = Anorthite, B = Baddeleyite, C = Corundum, Cr = Cristobalite, M = Mullite, Q = Quartz, Tz = Tetragonal zirconia)

Chemical composition of the two powders, determined by X-ray fluorescence (XRF, Rigaku ZSX 100E, Tokyo, Japan), is reported in Table 1. XRF results are in line with XRD analysis, confirming the aluminosilicate nature of chamotte and the presence of alumina, zirconia and silica in the AZS powder. Indeed, chamotte is mainly composed of  $\text{Al}_2\text{O}_3$  and  $\text{SiO}_2$  (these two oxides account for 96.40% of the total composition) while in AZS powder the main constituent is  $\text{ZrO}_2$  (43.90%) followed by  $\text{Al}_2\text{O}_3$  and  $\text{SiO}_2$  (54.20%). Considering that no silica containing compounds were determined in the XRD pattern of AZS powder, all the contained silica (19.60%) is present as an amorphous phase, as an important feature in the alkaline activation process. A small amount ( $< 1\%$ ) of  $\text{Fe}_2\text{O}_3$  is present in both powders.

**Table 1:** Chemical composition of refractory waste powders determined by XRF analysis (wt%)

Oxide	CH	AZS
$\text{Al}_2\text{O}_3$	59.60	34.60
$\text{SiO}_2$	36.80	19.60
$\text{ZrO}_2$	1.08	43.90
$\text{CaO}$	1.25	-
$\text{Fe}_2\text{O}_3$	0.93	0.23

Particle size distribution of raw powders was determined using a laser granulometer (Mastersizer 3000, Malvern Panalytical, Worcestershire, UK) after dispersion in ethanol. Figure 2 reports frequency and cumulative frequency of as-received CH and AZS. Even if CH particles are slightly finer than AZS ones, the

two raw powders present a similar bimodal particle size distribution. Particle sizes corresponding to 10, 50 and 90% of the cumulative distribution are given in Table 2.

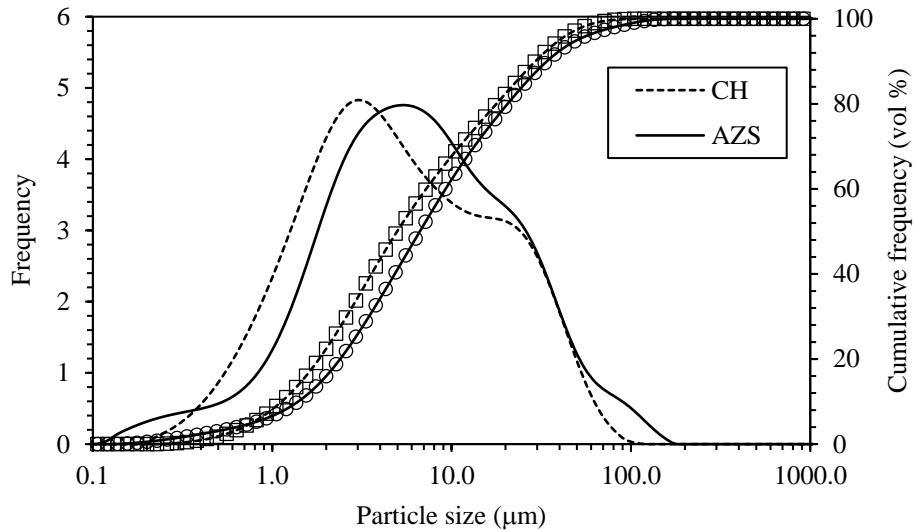


**Figure 2:** Particle size distribution of CH and AZS raw powders

**Table 2:** Particle sizes at 10% ( $d_{10}$ ), 50% ( $d_{50}$ ) and 90% ( $d_{90}$ ) of the cumulative distribution for CH and AZS raw powders

Powder	$d_{10}$ ( $\mu\text{m}$ )	$d_{50}$ ( $\mu\text{m}$ )	$d_{90}$ ( $\mu\text{m}$ )
CH	$1.06 \pm 0.01$	$4.66 \pm 0.06$	$27.52 \pm 0.64$
AZS	$1.21 \pm 0.01$	$6.25 \pm 0.22$	$31.84 \pm 2.37$

FE-SEM micrographs of CH particles are depicted in Figure 3. Fine particles (few microns in size) can be easily observed, in agreement with laser granulometry data (Table 2). Such particles are characterized by irregular shapes (Figure 3a) probably due to the grinding process; at higher magnification (inset of Figure 3b) primary particles, whose size is in the nanometric range, are visible as well.

AZS particles are depicted in Figure 4. Also in this case we can observe the irregular shape of particles and a size distribution coherent with granulometric data. In fact, few larger particles, whose size is in the range 10-20  $\mu\text{m}$ , are clearly visible (Figure 4a), while numerous fines ( $d < 5 \mu\text{m}$ ) are present onto bigger aggregates surface (inset of Figure 4a). The micrographs obtained in back-scattered mode (Figure 4b) allow distinguishing the main compounds present in AZS powder, i.e. zirconia (white areas) and alumina/silica (grey areas). The morphology of AZS powder can be ascribed to the production process of these refractories,

i.e. electrofusion. The two crystalline phases (i.e. corundum and zirconia) are interlocked and embedded in the glassy phase (i.e. silica). For this reason, melted cast AZS refractories have no open porosity [48], in agreement with our microscopic observations.

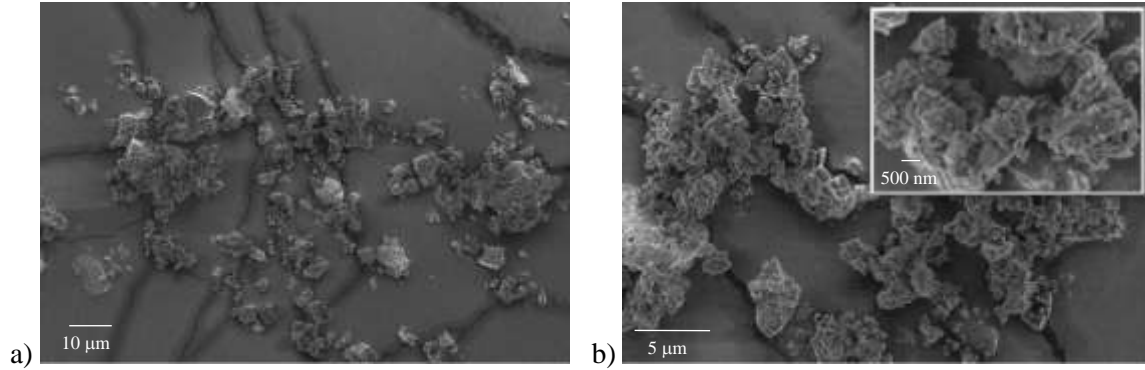


**Figure 3:** CH powder at different magnifications

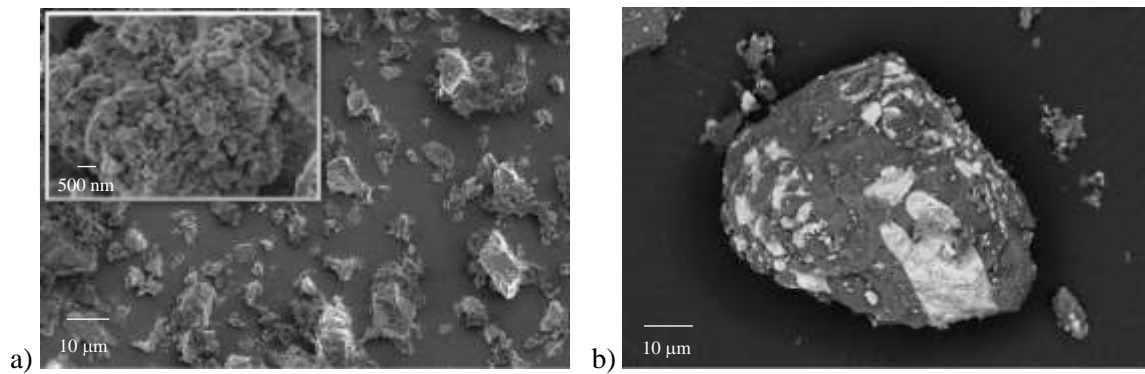


**Figure 4:** AZS powder at different magnifications a) and b) BSE micrograph

Alkaline activator used in this investigation was composed of sodium hydroxide (NaOH, purity > 98%, pellets, Sigma Aldrich), sodium silicate solution (density = 1.37 g/mL, pH 11.45, SiO<sub>2</sub> = 28.00%, Na<sub>2</sub>O = 8.28% and H<sub>2</sub>O = 63.72%, Ingessil S.r.L., Montorio, Italy) and distilled water.

## 2.2 Samples preparation

The alkaline solution was prepared dissolving NaOH pellets in distilled water for 2 hours before sodium silicate addition. Then, the solution was stirred for two additional hours prior to use. A fixed SiO<sub>2</sub>/Na<sub>2</sub>O molar ratio of 1.65 was used, according to previous studies [5,7].



Pastes were prepared by mechanically mixing CH or AZS with the alkaline solution in a laboratory mixer (Hobart, Columbus, OH, USA). Liquid to solid volume ratio (L/S) was fixed at 35/65 for CH-based pastes and at 38/62 for AZS-based pastes (corresponding to mass ratio of 0.25 and 0.23, respectively), according to preliminary tests aiming to optimize pastes workability. In fact, viscosity of the pastes was determined using a viscometer (Brookfield HBDV-II) at different shear rates (from 10 to 200 rpm). In both cases, a shear-thinning behavior was observed (Figure 5), more pronounced in the case of AZS-based paste.

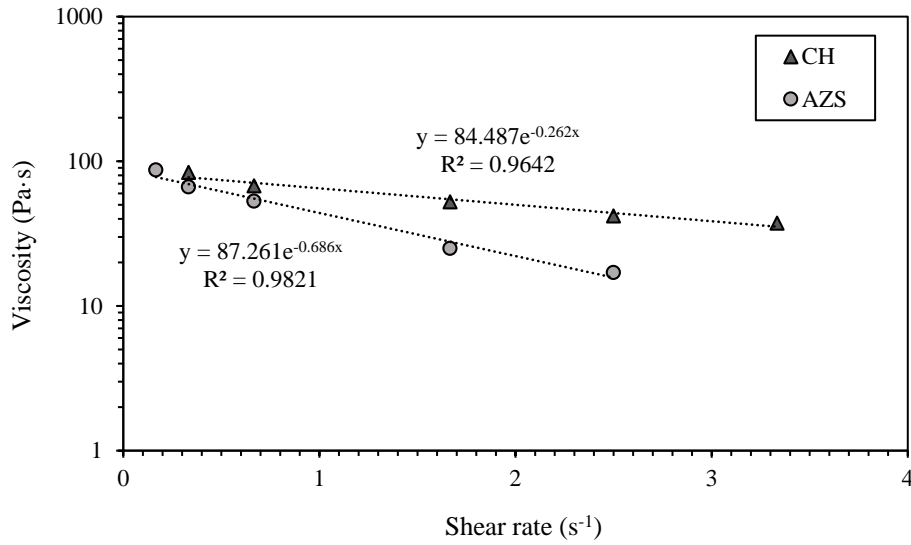


**Figure 5:** Viscosity of fresh pastes obtained by mixing CH and AZS powders by the alkaline activator

Finally, pastes were cast into PMMA molds to obtain prismatic samples ( $2 \times 2 \times 8 \text{ cm}^3$ ) for mechanical tests. Alkali-activated pastes were oven-cured for 24 hours at  $60 \text{ }^\circ\text{C}$  in sealed vessels before specimens demolding. Then, samples were cured for 28 days in closed containers at constant relative humidity and temperature ( $\text{RH} = 95 \pm 2 \%$  and  $20 \pm 3 \text{ }^\circ\text{C}$ , respectively). Finally, samples were exposed to four different temperatures (800, 1000, 1200 and  $1400 \text{ }^\circ\text{C}$ , respectively) in an electric furnace (Nabertherm GmbH, Germany). In order to avoid cracking, samples were heated at  $2 \text{ }^\circ\text{C}/\text{min}$  up to  $100 \text{ }^\circ\text{C}$ , and then at  $5 \text{ }^\circ\text{C}/\text{min}$  up to the maximum temperature, followed by a dwell of 30 min. Then, specimens were left in the furnace to cool down gradually to room temperature. Alkali-activated pastes (AA) are labelled according to raw powders and firing temperature: for example, AA-CH\_1200 is the CH-based alkali activated paste, exposed at  $1200 \text{ }^\circ\text{C}$ .

### 2.3 Samples characterization

TG-DTA analysis (Netzsch STA 409 C/CD, Selb, Germany) were performed on powdered samples, up to 1500 °C, in air (heating rate of 10 °C/min, air flow 100 mL/min).

XRD analysis was performed on powdered samples (before and after high-temperature exposure) and spectra were recorded using a Pan'Analytical X'Pert Pro instrument (Pan'Analytical, Almelo, The Netherlands) with CuK $\alpha$  radiation (0.154056 nm) in the 2 $\theta$  range 10-70°.

Specimens linear expansion or contraction was measured after thermal treatment using a digital caliper. The results are the average values of three different measured specimens.

Hardened pastes were submitted to both flexural and compressive tests. Strength was determined on both as-cured samples (after 28 days of curing) and after exposure to the different temperatures. The unfired samples (named AA-CH and AA-AZS, respectively) were used as a reference. Flexural strength was measured using an electromechanical testing system (Shimadzu AGS-X, Kyoto, Japan) equipped with a load cell of 10 kN in three-point bending mode. After flexural tests, specimens were cut with a diamond blade (to obtain cubes 2×2×2 cm<sup>3</sup>) for compressive tests. Compressive strength was measured using an electromechanical testing system (Lloyd LR150K, Bognor Regis, UK) equipped with a load cell of 150 kN. The results are the average of three measurements for flexural tests and of six measurements for compressive tests.

FT-IR measurements were performed on a Thermo-Nicolet 6700 Spectrometer (Thermo Fisher Scientific, Massachusetts, USA). Spectra were recorded in attenuated total reflectance (ATR) mode in the range 4000-400 cm<sup>-1</sup> with a resolution of 4 cm<sup>-1</sup> using a diamond crystal. Baseline correction and spectra normalization were performed for all the investigated samples.

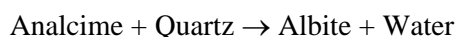
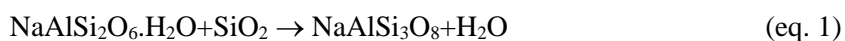
Pores size distribution was investigated via Mercury Intrusion Porosimetry (MIP) using a AutoPore IV 9500 mercury porosimeter (Micromeritics, Georgia, USA) from pressure 0.07 to 413.69 MPa.

Morphologies of powders and alkali-activated pastes (on polished surfaces) were examined by means of a FE-SEM (Zeiss Supra-40, Oberkochen, Germany) equipped with an Oxford Energy Dispersive X-ray detector. All observations were performed after sputtering samples with a thin coating of platinum (for CH-based materials) and chromium (for AZS samples).

### 3. Results and Discussion

#### 3.1 XRD

XRD patterns of as-prepared and fired CH and AZS-based pastes are reported in Figure 6 and Figure 7, respectively. No meaningful differences, in terms of new crystalline phases, can be observed by comparing CH raw powder (Figure 1a) and the unfired AA-CH sample (Figure 6a). However, in this last case, traces of zeolitic phases (analcime, sodium aluminum silicate hydrate JCPDS file n°00-041-1478,  $\text{NaAlSi}_2\text{O}_6 \cdot \text{H}_2\text{O}$ , N-A-S-H) can be detected. On the contrary, when AA-CH is exposed to high-temperature, some differences in the XRD patterns can be recognized, as better evidenced in Figure 6b, focusing on the 18-44 ( $^\circ$ )  $2\theta$  range. We can observe, in fact, a progressive increase of corundum peaks intensity (see for instance the peak located at  $2\theta = 43.36$  in Figure 6b) by increasing the exposition temperature. Moreover, at 1400  $^\circ\text{C}$ , all the patterns corresponding to the andalusite phase disappear. According to literature [20,49], andalusite ( $\text{Al}_2\text{O}_5\text{Si}$ ) decomposition leads to the formation of amorphous silica and extra-alumina phase, because the presence of a liquid phase avoids andalusite mullitization in this temperature range [20,49]. The sample AA-CH\_1000 presents some new crystalline phases; in particular, the peaks corresponding to aluminum sodium silicate ( $\text{AlNaO}_4\text{Si}$ , JCPDS file n°00-002-0625) and sillimanite ( $\text{Al}_2\text{SiO}_5$ , JCPDS file n°00-038-0471) can be detected (Figure 6b), while these phases are no more present at 1200 $^\circ\text{C}$ . Sillimanite is one of the three  $\text{Al}_2\text{SiO}_5$  aluminosilicate polymorphs and can be formed from andalusite at ambient pressure at approximately 750  $^\circ\text{C}$ . Accordingly, a small signal corresponding to sillimanite phase can be already detected at 800  $^\circ\text{C}$ , even its presence can be more easily detected at 1000 $^\circ\text{C}$ . Moreover, it is possible to observe an increase of the albite signal by increasing the exposure temperature, up to 1400  $^\circ\text{C}$ , when the albite peaks disappear, probably due to melting [51]. The increase of albite signal can be imputed to the following reaction, which describes the transformation of analcime into albite [52,53]:



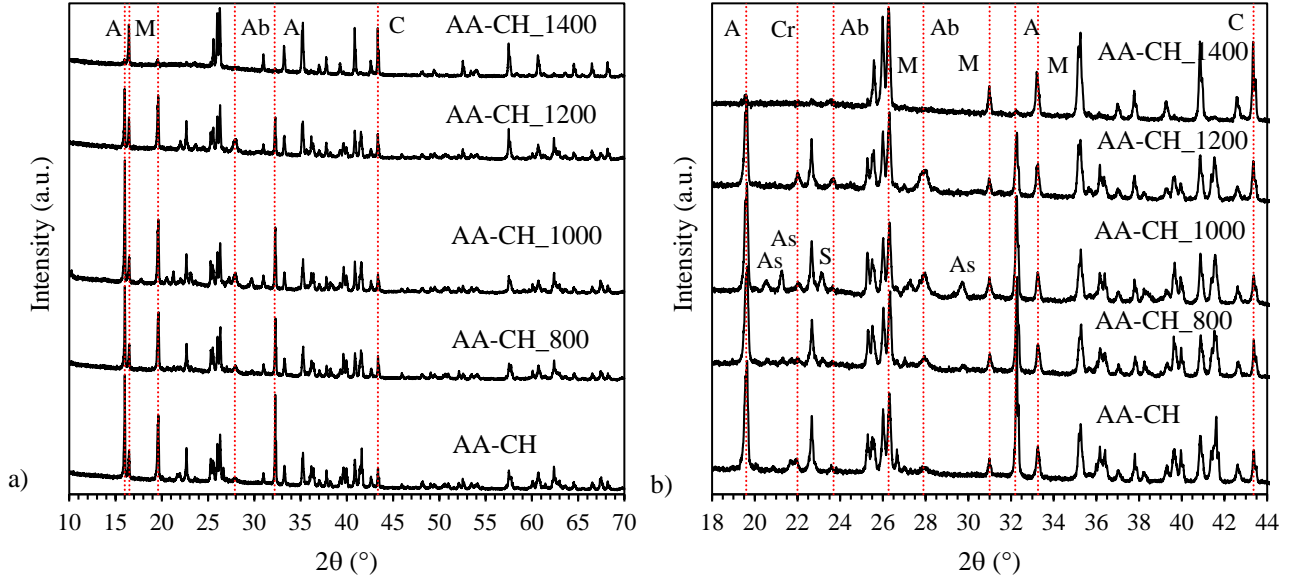
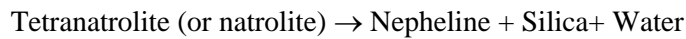
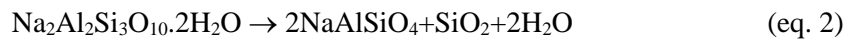


**Figure 6:** XRD patterns of unfired and fired AA-CH pastes in the 10-70 (a) and 18-44 (b)  $2\theta$  range (A = Andalusite, Ab = Albite, As = Aluminum Sodium Silicate, C = Corundum, Cr = Cristobalite, M = Mullite, S = Sillimanite)

Also for AZS-based pastes, no meaningful differences can be detected by comparing the XRD patterns of the raw powder (Figure 1) and the unfired AA-AZS paste (Figure 7a). However, in this last sample, traces of the zeolite tetranatrolite ( $\text{Na}_2\text{Al}_2\text{Si}_3\text{O}_{10} \cdot \text{H}_2\text{O}$ , JCPDS file n°00-029-1166) are present, thus indicating a reaction between the alumina-rich raw powder and the strong sodium-silicon-based alkaline solution, suggesting the possible occurrence of a geopolymer reaction. Considering phases evolution at increasing exposure temperatures, the appearance of nepheline ( $\text{AlNaO}_4\text{Si}$ , JCPDS file n°00-035-0424) at 1000 °C is highlighted in Figure 7b, which depicts the XRD patterns in the 20-32 (°)  $2\theta$  range. Formation of nepheline and amorphous silica, between 800 and 1000 °C, can be imputed to tetranatrolite decomposition, according [54] and [55]:



The formation of nepheline further strengthens the hypothesis of alkaline-activation reactions in the paste: in particular, it can be imputed to dehydration and recrystallization processes of N-A-S-H and/or zeolites phases at high temperatures, as previously observed in literature [27,56].

Moreover, at increasing exposure temperatures, a shift toward lower  $2\theta$  angles (meaning an increase of d-spacing) of corundum and baddeleyite peaks was observed, as highlighted in Figure 7b, which depicts the XRD patterns in the 25-35 ( $^{\circ}$ )  $2\theta$  range. This behavior can be explained considering that at increasing exposure temperature, zirconia and alumina lattices expand and ions (mainly  $\text{Na}^+$ ) can penetrate in the lattice structure [57].

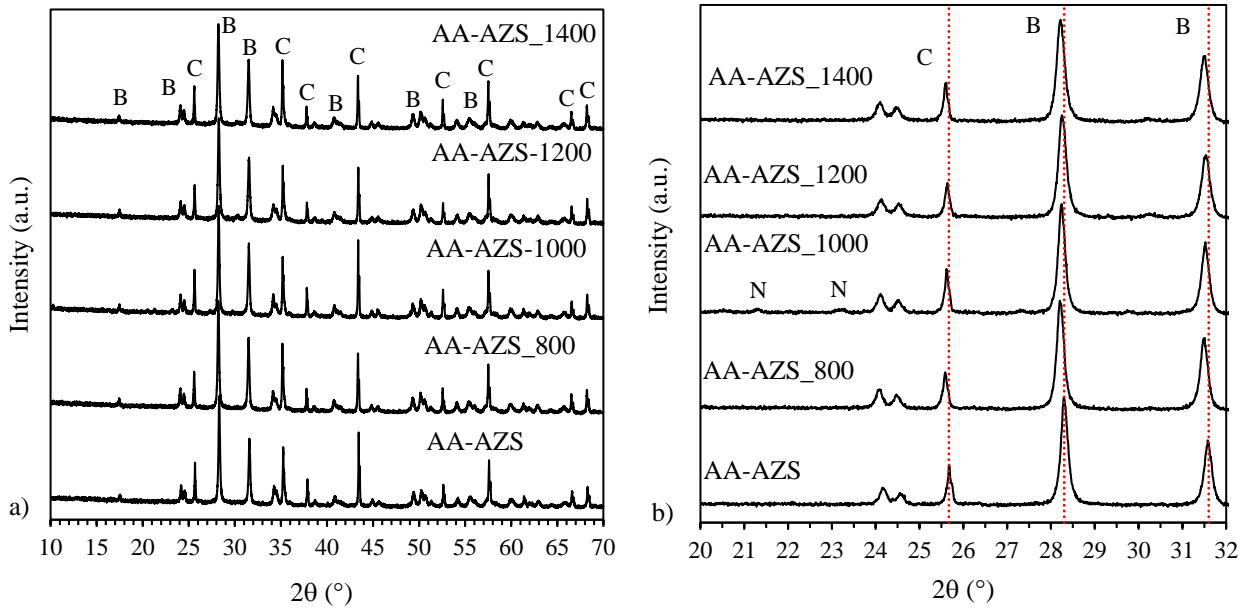


**Figure 7:** XRD patterns of unfired and fired AA-AZS samples in the 10-70 (a) and 20-32 (b)  $2\theta$  range (B = baddeleyite, C = corundum, N = nepheline)

### 3.2 Thermal properties

Cement-based materials display a very high mass loss when heated, due to hydrated compounds decomposition [58]. In order to assess the high-temperature behavior of the AA-paste, TGA-DTA analysis were performed up to 1500  $^{\circ}\text{C}$ , and compared to those of raw powders.

TGA-DTA of CH and AA-CH-based paste are reported in Figure 8 and Figure 9, respectively. Chamotte powder shows only a slight mass loss (0.83%) in the investigated temperature range, mostly due to physically adsorbed water, corresponding to the first endothermic signal of the DTA curve. Then, other two endothermic phenomena are visible at 744  $^{\circ}\text{C}$  and 1217  $^{\circ}\text{C}$ , respectively. According to XRD data, the first one could be imputed to the andalusite-sillimanite transformation, while the latter correspond to andalusite decomposition into  $\alpha\text{-Al}_2\text{O}_3$  and amorphous silica. As regard to AA-CH, a total mass loss of 6.31% was

determined up to 1500°C (5.40% up to 350 °C), showing a very high thermal stability compared to cementitious materials [58]. The first endothermic peak, centered at 102 °C, can be attributed to physically adsorbed water evaporation; the shoulder, at approx. 300 °C, is due to dehydration of zeolitic water presents in the analcime phase determined in the XRD pattern of AA-CH. Indeed, analcime endothermal dehydration occurs in the range 150-400 °C [53]. The broad endothermic DTA signal centered at 495 °C can be attributed to the glass transition of amorphous sodium silicate [72,73]. Then, the exothermic peak at 685 °C can be associated to the formation of aluminum sodium silicate observed in the XRD pattern of AA-CH\_1000. Finally, two endothermic signals can be detected at 1133 °C and 1258 °C, respectively. The former can be related to the melting of albite [50], in partial agreement with XRD data showing the albite signal up to 1200°C. The latter can be attributed to andalusite decomposition [59], in line with XRD data (Figure 6), showing the disappearance of this phase in the 1200-1400 °C range.

Considering AZS raw powder, no weight loss occurs in the whole investigated temperature range (Figure 9). The DTA curve does not present significant signals, apart from a small endothermic peak, at 1149 °C, which can be imputed to zirconia transformation from monoclinic to tetragonal phase [60]. The AA-AZS- paste showed a lower mass loss (4.68 % at 1500 °C, being the 4.23 % mass loss recorded up to 350 °C) compared to AA-CH. Also in this case, an endotherm related to loosely bound water evaporation (at approx. 100 °C) and a shoulder at about 200 °C corresponding to zeolites dehydration are present. Also in this case, an endotherm signal is recognizable at 495 °C and is due to the glass transition of amorphous sodium silicate [72,73]. Two endothermic phenomena are recognizable at approximately 970 and 1150 °C, respectively. The first one can be related to tetranatrolite devitrification (eq. 2), while the second one is representative of the zirconia martensitic transformation, as already observed in the raw powder.

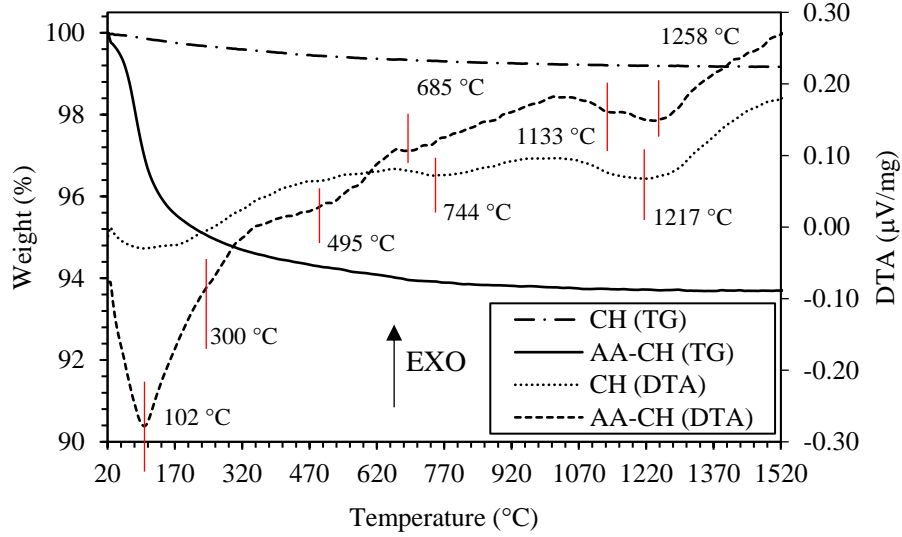


**Figure 8:** TGA-DTA of CH and AA-CH paste

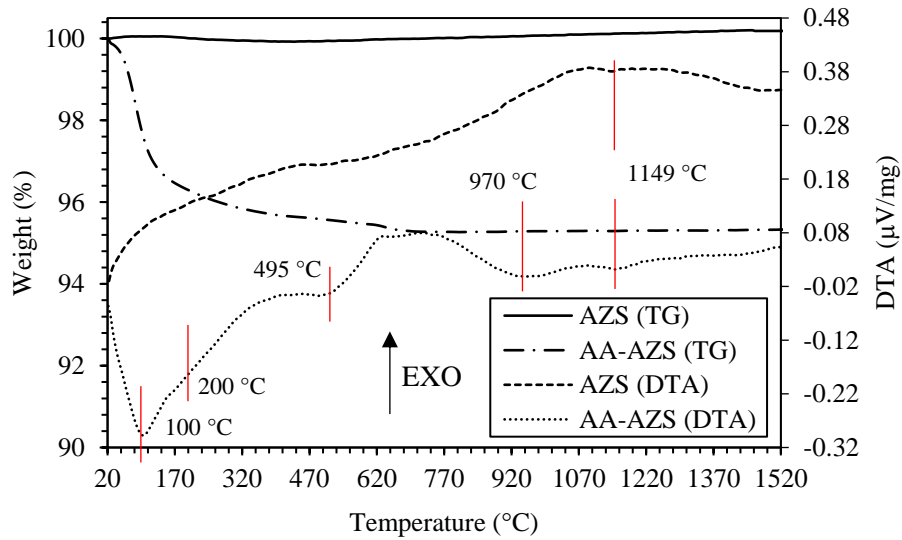


**Figure 9:** TGA-DTA of AZS and AA-AZS paste

### 3.3 FT-IR

FT-IR spectra of unfired and fired AA-CH pastes are compared to the raw powder. For sake of clarity, only the 500-1200  $\text{cm}^{-1}$  range is depicted in Figure 10a. The peaks in the wavenumbers range 800-1200  $\text{cm}^{-1}$  are related to Si-O-Si and Si-O-Al bond vibrations typical of geopolymers [26,61,42,62]. Moreover, the peaks at 775  $\text{cm}^{-1}$  and 605  $\text{cm}^{-1}$  correspond to  $\text{AlO}_4$  tetrahedra and  $\text{AlO}_6$  octahedra vibrations, respectively. Finally, the peak at 685  $\text{cm}^{-1}$  corresponds to  $\text{AlO}_5$  present in andalusite [63,64]. At increasing exposure temperature,

the three peaks at 974, 933 and 892  $\text{cm}^{-1}$  progressively disappear. Similarly, also the peak located at 775  $\text{cm}^{-1}$  disappears for the sample exposed to the highest exposure temperature (i.e. 1400  $^{\circ}\text{C}$ ). Finally, a broadening of the peaks at 602 and 1100-1200  $\text{cm}^{-1}$  is also visible. All these modifications are coherent with the disappearance of the andalusite phase, as determined with XRD analysis (Figure 6), and the progressive increase of amorphous silica.

AZS raw powder (Figure 10b) presents three main signals at 1050, 625 and 500  $\text{cm}^{-1}$ , representative of oxygen atoms vibrations in the  $\text{SiO}_2$  structure [5], Al-O groups stretching of alumina [70] and monoclinic  $\text{ZrO}_2$  Zr-O vibrations [71], respectively. Alkali-activated pastes before and after firing present a shift toward lower wavenumbers of Al-O signals, indicating the decrease of long-range order of crystalline phases. Considering AZS-based pastes, no meaningful differences are recognizable among the samples exposed to the different temperatures (Figure 10b), coherently to XRD analysis (Figure 7).

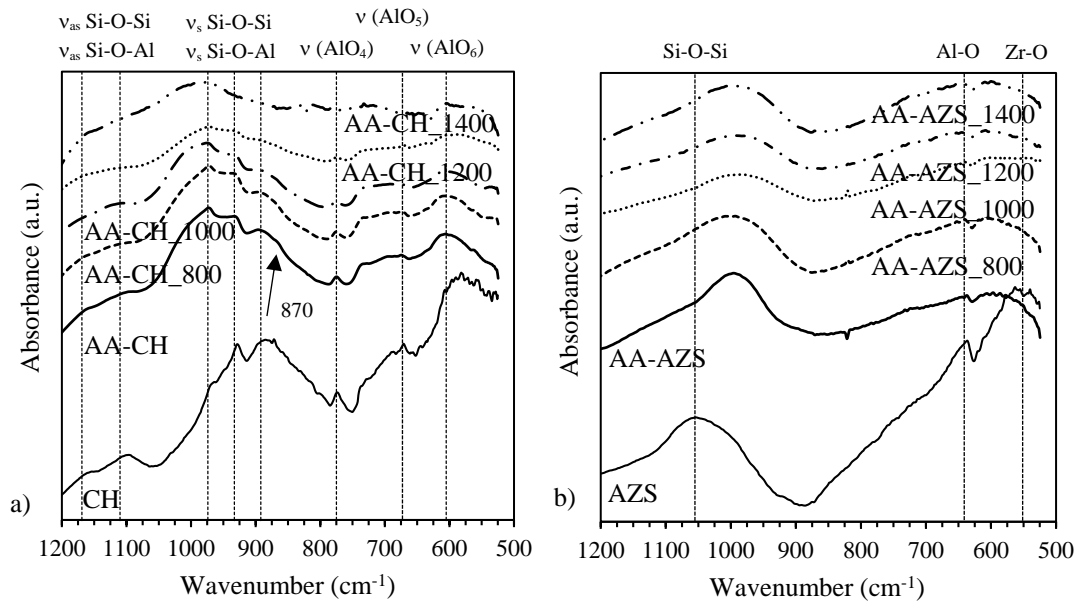


**Figure 10:** FT-IR spectra (500-1200  $\text{cm}^{-1}$ ) of a) CH and AA-CH pastes and b) AZS and AA-AZS pastes



### 3.4 Physical properties

The linear variations of the AA-CH and AA-AZS pastes are reported in Figure 11 as a function of exposition temperature. As evident, two different behaviors can be recognized: AA-CH samples shrink up to 1200 °C and expand between 1200 and 1400 °C; on the contrary, AZS alkali-activated pastes expand up to 1000 °C, then shrink between 1000 and 1200 °C and slightly expand again between 1200 and 1400 °C. In both cases, the highest linear contraction (2.10 and 4.89% for AA-AZS and AA-CH, respectively) was measured at 1200 °C, meaning that at this temperature sintering occurs [31,65]. The high-temperature shrinkage (up to 1200°C) which characterizes the AA-CH samples has been already observed in literature for geopolymers, even if specific thermal behaviors strongly depend on raw powders, curing conditions, activator nature and composition [29,30,61,65]. For instance, Duxon et al. [65] showed a very important volumetric contraction up to 1000°C in metakaolin-derived geopolymers (between 8 and 20 vol%, as a function of the Si/Al ratio within the specimens), while such volumetric shrinkages were almost doubled (in the range ~16 and 40 vol%) for metakaolin-based samples determined by Bernal et al. [29]. However, these authors observed a significant decrease of volumetric contraction by adding refractories particles and fibers to MK-matrix. For granulated blast furnace slag derived geopolymers, Rovnaník et al. [61] reported linear shrinkages of about 7% up to 1200°C. In all cases, the observed contractions were correlated to materials dehydration and dihydroxylation in the 200-500°C temperature range, while at 800°C-1000 °C the shrinkage was mainly related to softening and viscous sintering, accompanied by structural rearrangement [29]. The contraction here observed, in spite significant, was however lower than those reported in the previously mentioned investigations. In fly-ashes derived geopolymers, Carabba et al. [27] observed a slight linear shrinkage up to 700°C, followed by an expansion up to 800°C, in line with the trend we observed, even if displaced at lower temperatures. While the contraction was associated to materials densification, the expansion was imputed to the bloating of residual silicate phases and/or crack formation, being these phenomena hindered by the addition of refractory particles. This observation is in agreement with our results, showing the presence of inner voids and cracks in samples fired at 1400°C. Moreover, in our samples, between 1200 and 1400 °C andalusite decomposition and increase of glassy phase occur, further explaining the linear expansion. A completely different trend was observed in AA-AZS pastes, up to 1000 °C: in fact, we can observe a linear thermal expansion till this temperature. Then, in agreement with AA-CH pastes, a significant shrinkage

occurs in the 1000 °C-1200 °C temperature range, due to material densification, followed by a slight expansion up to 1400 °C. At about 1150°C, zirconia transformation from monoclinic to tetragonal phase occurs, accompanied by a significant contraction [66]. However, as this martensitic transformation is reversible, a corresponding expansion during cooling occurs, thus not providing overall effect on final materials volumetric changes [66]. As a proof, the XRD data of the fired samples show only traces of tetragonal zirconia, in line with the starting content in AZS raw powders. In this case, no meaningful defects were recognized in the samples after firing, even at the highest investigated temperature.

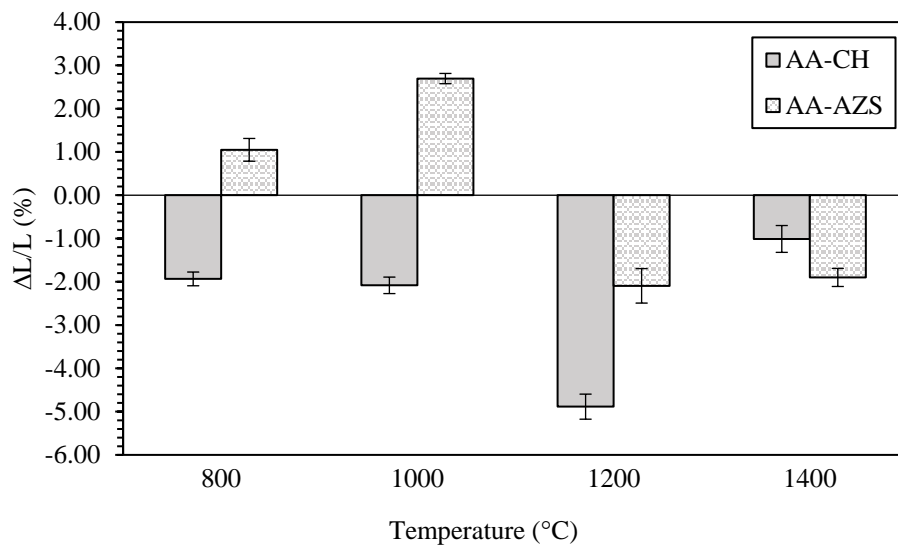


**Figure 11:** Linear variation of AA-CH and AA-AZS pastes after exposure to high temperatures (positive variations are expansions)

To evaluate the effects of firing temperature on the macroscale appearance of the alkali-activated pastes, some pictures of the alkali-activated samples, AA-CH and AA-ASZ, are reported in Figure 12 and Figure 13, respectively. No meaningful variations can be observed on AA-CH samples after firing at 1200 °C (Figure 12b) compared to the unfired sample (Figure 12a). However, a further increase of temperature (i.e. 1400 °C) leads to cracks appearance (Figure 12c), as previously stated. On the contrary, firing temperature didn't affected, macroscopically, AA-AZS samples (Figure 13).

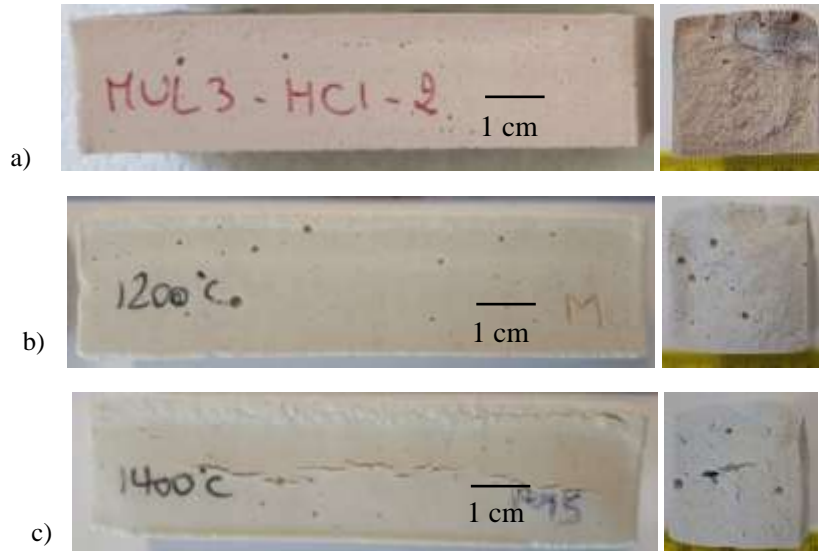


**Figure 12:** AA-CH samples (side view and cross section) a) before and after exposure at b) 1200 °C and c) 1400 °C

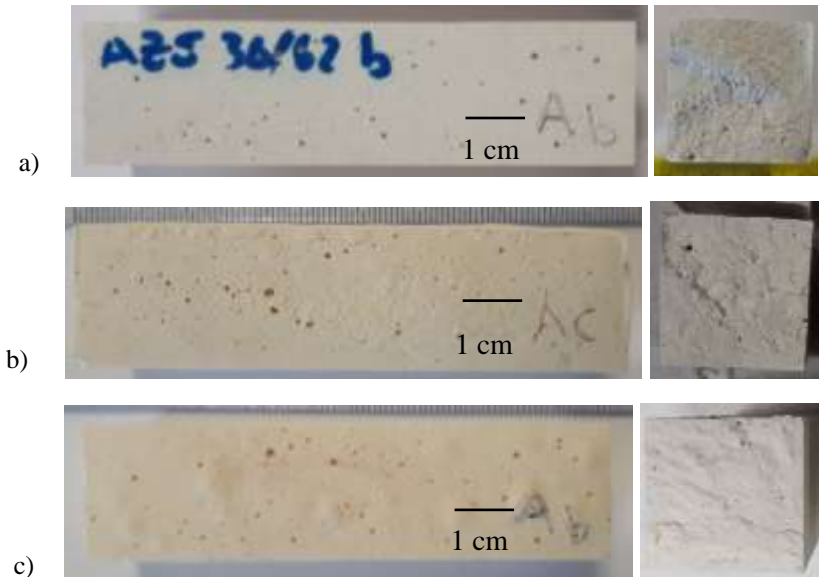


**Figure 13:** AA-AZS samples (side view and cross section) a) before and after exposure at b) 1200 °C and c) 1400 °C

Porosity, pore size distribution and density of AZS and chamotte-based pastes were measured using mercury intrusion porosimetry. Porosity (divided in macropores ( $d > 1 \mu\text{m}$ ), mesopores ( $1 < d < 0.1 \mu\text{m}$ ) and micropores ( $d < 0.1 \mu\text{m}$ )), bulk and apparent density are reported in Figure 14 and Figure 15 for AA-CH and AA-AZS samples, respectively. Concerning the total porosity (i.e., the sum of macro, meso and micropores), both samples showed an increase between as-prepared pastes and after exposure to 800 and 1000 °C, due to water loss and glassy phase densification. However, such increase was much more important in AA-AZS samples, since the total porosity almost doubled from the unfired ( $\sim 11 \text{ vol\%}$ ) to 1000 °C-fired sample ( $\sim 22 \text{ vol\%}$ ),

being this increase responsible for material expansion observed in Figure 11. Then, moving from 1000 to 1200 °C, a sharp decrease of porosity was observed in both cases, thanks to the shrinkage occurring during the sintering process (Figure 11). Finally, in the case of AZS samples, porosity was stable between 1200 and 1400 °C (6 and 5%, respectively). On the contrary, for CH-based samples, porosity slightly increased moving from 1200 to 1400 °C (11 and 14%, respectively), probably due to andalusite decomposition and material expansion. Anyway, AA-AZS samples show a lower porosity almost for all the investigated temperatures compared to AA-CH ones, in line with the highly dense nature of CH raw particles.

As regard pore classes, in AA-CH-based samples (Figure 14), a very small amount of micropores was detected for all the investigated samples, except for AA-CH\_1200 sample. AA-CH, AA-CH\_800 and AA-CH\_1000 are predominantly composed of mesopores, which decrease at 1200°C and almost disappear at 1400°C, while macropores are formed. Macropores increase moving from 1200 °C to 1400 °C-fired samples is consistent with the volumetric expansion of these two samples. Unfired AA-AZS sample shows almost the same volume of micro, meso and macropores (3, 5 and 3%, respectively, Figure 15). Then, a severe increase of macropores was determined in AA-AZS\_800 and AA-AZS-1000 (+248 and 434%, respectively) while mesopores were constant and micropores slightly decreases at increasing temperature. Finally, the porosity of samples fired at 1200 and 1400 °C is mainly composed of macropores, while micro and mesopores disappear, according to what previously discussed about high-temperature sintering and shrinkage of AZS-based materials (Figure 11).

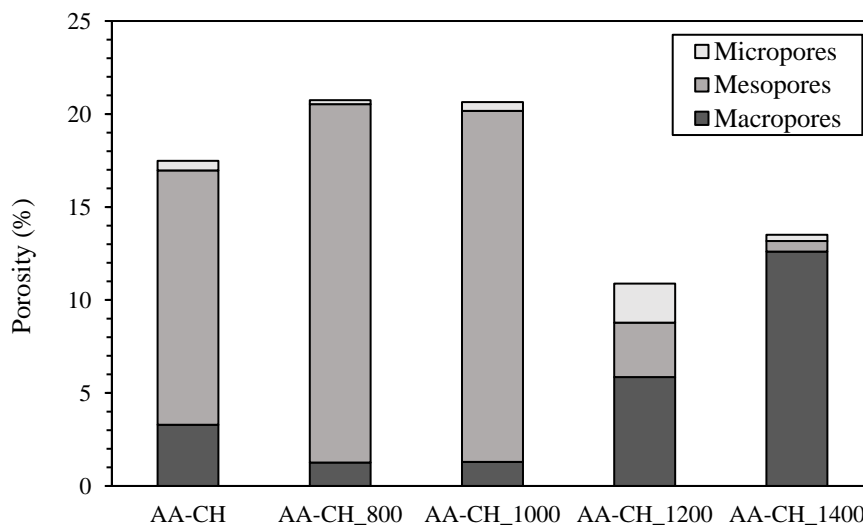


**Figure 14:** Porosity and pores distribution of AA-CH pastes before and after high-temperatures exposure

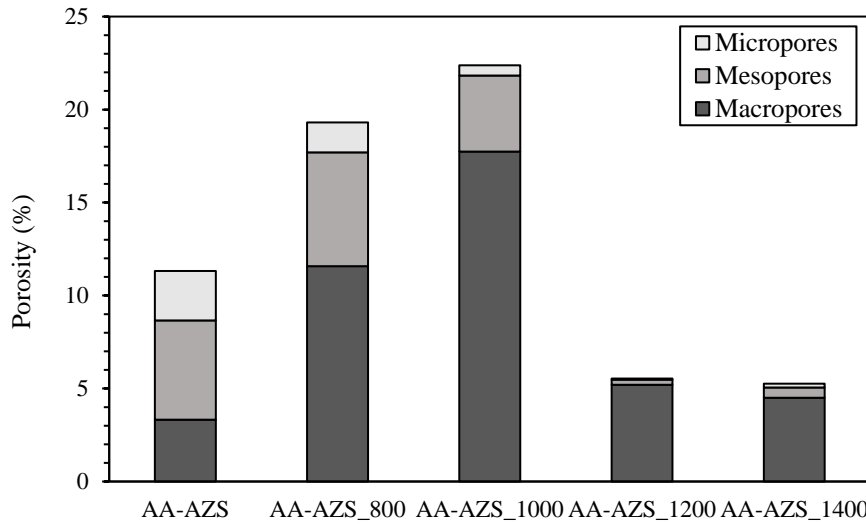


**Figure 15:** Porosity and pores distribution of AA-AZS pastes before and after high-temperatures exposure

### 3.5 Mechanical properties

Flexural and compressive strength of as-prepared and high temperatures-exposed AA-CH and AA-AZS samples are reported in Figure 16 and Figure 17, respectively.

The first, very important result here achieved concerns the very high mechanical properties of the unfired alkali-activated samples, particularly under compressive test: values as high as ~ 60 and 70 MPa are respectively reached by AA-AZS and AA-CH samples. Such results strengthen the hypothesis – supported by XRD and FTIR data, that alkaline activation phenomena occurred in the materials, with the formation of an effective binder phases joining the refractory, partially reacted particles. We wish to point out that, while some previous investigation relates to the use of chamotte as filler or aggregate in geopolymers based materials [28,30,34], the exploitation of AZS refractory fines in these kinds of materials is totally new in literature. As a further important result, we can observe that all fired materials present a significant improvement of both flexural and compressive strength after high-temperature firing. In the case of AA-CH pastes (Figure 16), we can observe a neat increase of the flexural strength from the as-prepared to all fired samples, whose strengths were comparable. Compressive strength followed a similar trend, with the maximum value (> 200 MPa) achieved after firing at 1200 °C. AA-CH\_1400 showed a certain decrease respect the previous temperatures, due to the formation of some cracks and voids within the samples, as already mentioned, which affected the mechanical strength.

In case of AA-AZS samples (Figure 17), flexural and compressive strength showed two remarkable increases: the former, from unfired material to 800 °C and 1000 °C-fired samples; the latter, after firing at both 1200 °C and 1400 °C, where compressive strength close to 180 MPa were achieved. The first increase can be ascribed to the melting of the glassy phase that binds together AZS particles; the second to the sintering process.

Our results represent a significant advancement as respect to previous literature where, generally, a decrease of mechanical properties is observed after high-temperature exposure of alkali-activated samples [13,25-29,42,43,61,67,69]. Only few authors reported a compressive strength increase [27,62,69]. Even if direct comparisons are difficult to perform, due to huge variety of compositions and processing parameters, Table 3 summarizes the key features of some recent papers dealing with high-temperature exposure of alkali-activated materials, in order to highlight literature results and the advances achieved in this research. Some recent papers dealing with high-temperature exposure of geopolymers are summarized in Table 3.

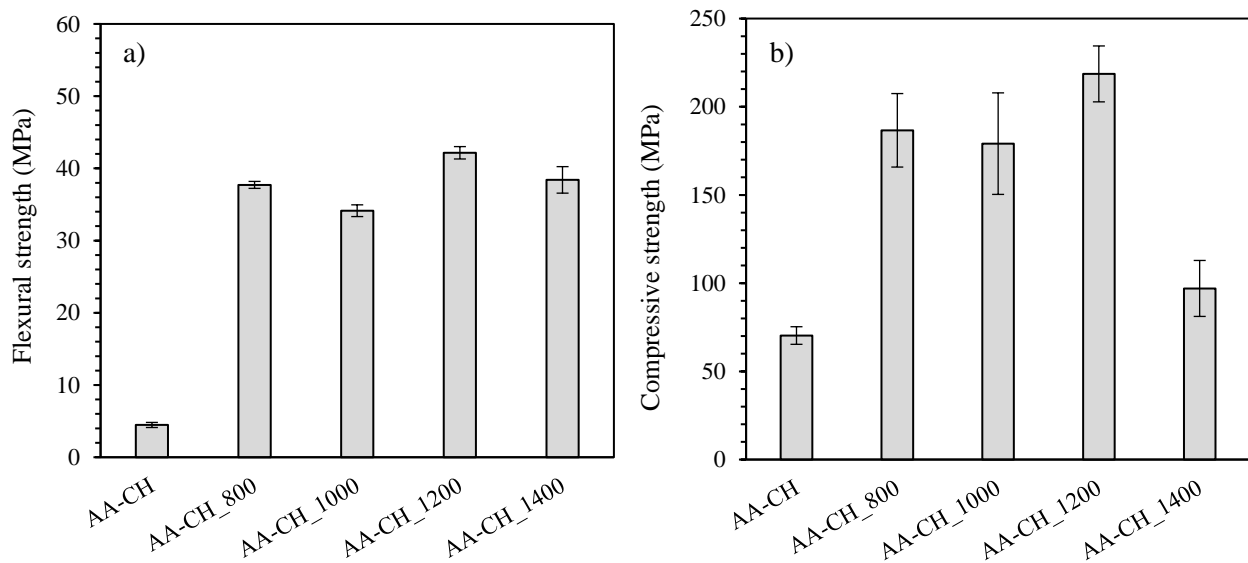


**Figure 16:** Flexural (a) and compressive (b) strength of unfired and fired AA-CH samples (bars represent  $\pm$  standard deviation of results)

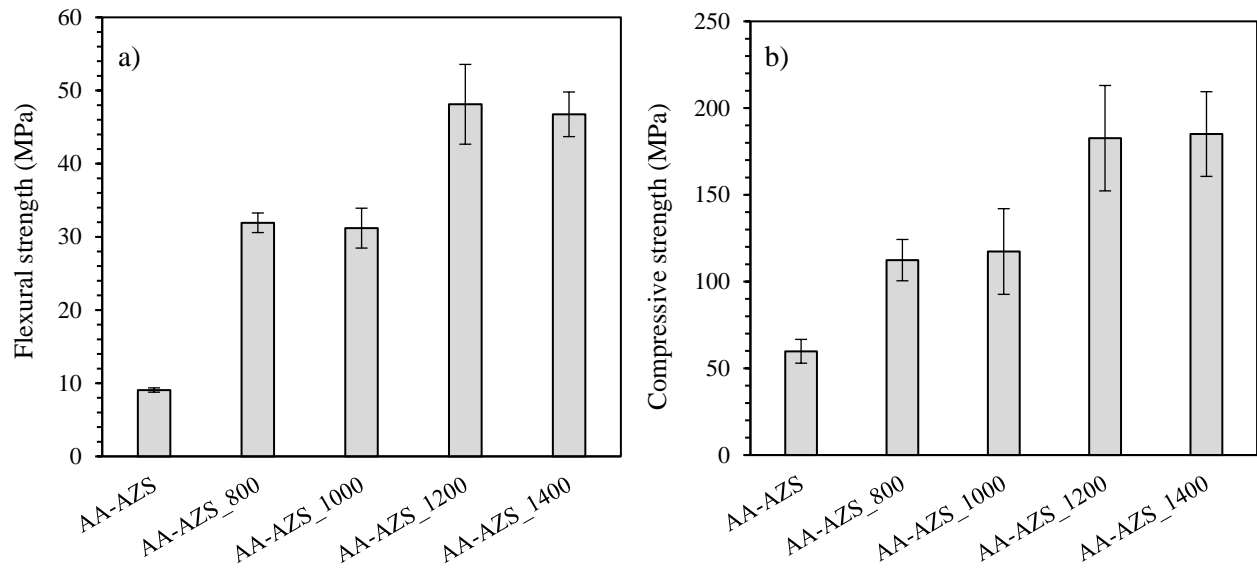


**Figure 17:** Flexural (a) and compressive (b) strength of unfired and fired AA-AZS samples (bars represent  $\pm$  standard deviation of results)

**Table 3:** Mechanical properties of different geopolymers after exposure to high-temperatures (literature results)

Raw powder	Exposure temperatures	Mechanical properties	Reference
GBFS	200, 400, 600, 800, 1000 and 1200 °C	Compressive strength decrease (approx. 15 % up to 600 °C; 70 % at 800 °C; 40 % at 1200 °C)	Rovnaník et al. (2013) [61]
MK and MK/FA-F	500, 750 and 1000 °C	Compressive strength decrease (approx. 80 % between 800 and 1000 °C for 100MK; 40 and 60 % at 1000 °C for 50MK 50FA-F and 75MK 25 FA-F, respectively)	Giosuè et al. (2019) [68]
MK and MK/Refractory particles	600, 800 and 1000 °C	Compressive strength decrease (approx. 80 % between 600 and 1000 °C for MK; 53 and 25 % for MK/RP composites at 600 °C; further decrease at 800 and 1000 °C)	Bernal et al. (2012) [29]
MK and MK/Cordierite	800 °C (thermal shock)	Compressive strength decrease (approx. 55 and 65 % after 5 and 15 cycles for samples containing 40 % of cordierite; 27 and 20 % after 5 and 15 cycles for 50 % cordierite samples)	Hemra et Aungkavattana (2016) [26]
MK, MK/SF, MK/GBFS, MK/Chamotte	100, 300, 500, 700 and 1000 °C	Compressive strength decrease for all the formulations (approx. 68 % at 1000 °C for MK/Chamotte that reported the lowest strength decrease)	Trindade et al. (2017) [32]
GBFS	200, 400, 600 and 800 °C	Slight compressive strength increase between 200 and 400 °C; significant compressive strength decrease between 600 and 800 °C.	Rashad et al. (2016) [43]
GBFS	200, 400, 600, 800 and 1000 °C	Compressive strength decrease up to 600 °C then a slight increase (but still lower than the reference sample, i.e. not thermally treated)	Rashad et al. (2016) [67]
MK/tabular alumina	600, 800, 1000 and 1200 °C	Compressive strength decrease at 600 °C then a slight increase between 800 and 1000 °C (but still lower than the reference sample, i.e. not thermally treated), further decrease at 1200 °C	Moosavi et al. (2019) [25]
GBFS	200, 400, 600, 800 and 1000 °C	Slight compressive strength increase up to 200 °C; significant compressive strength decrease between 400 and 600 °C. Only one formulation was tested after 800 °C (GBFS/RH, 5 MPa). None of the samples was mechanically tested after 1000 °C.	Bernal et al. (2015) [42]
FA/Refractory particles	800 and 1000 °C	Compressive strength increase (approx. 450 and 530 % after exposure at 800 and 1000 °C, respectively)	Carabba et al. (2017) [27]
OPC/Ferrochrome slag	100, 200, 300, 400, 500, 600, 700 and 800 °C	Compressive strength increase (approx. between 28 and 47 % at 800 °C, depending on the OPC content)	Mohabbi Yadollahi and Dener (2019) [62]
FA	100, 200, 300, 400, 500, 600, 700, 800, 900 and 1000 °C	Compressive strength increase (for the Eraring FA; approx. 230 % at 1000 °C)	Rickard et al. (2015) [69]



### 3.6 Microstructure and EDS analysis

FE-SEM micrographs of CH and AZS-based alkali activated pastes are reported in Figure 18 and Figure 20, respectively. In both cases, particles of the two starting powders can be still recognized, well embedded in a gel/matrix in which Al ions deriving from CH and AZS raw powders are dissolved, as assessed by EDS analysis (EDS maps not reported). Indeed, semi-quantitative analysis confirms the formation of a N-A-S-H gel and zeolitic phases discussed previously (XRD, DTA-TGA and FT-IR analysis). Microstructural and morphological variations after exposure to the different temperatures for CH and AZS-based pastes are reported in Figure 19 and Figure 21, respectively. FE-SEM micrographs confirm porosimetric results, showing an increase of porosity for both samples after exposure at 800 and 1000 °C, due to water evaporation and matrix rearrangement. Then, after exposure to 1200 °C, matrix densification occurs and porosity is significantly reduced. However, after exposure to 1200 and 1400 °C, an increase of the macropores ( $d > 10 \mu\text{m}$ ) is clearly recognizable, coherently to mercury intrusion porosimeter results (Figure 14 and Figure 15 for CH and AZS-based pastes, respectively). At higher magnifications (insets of Figure 19 and Figure 21), the progressive occlusion of the pores by the glassy phase is evident. Indeed, the softening and viscosity reduction of the glassy phase lead to the incorporation of CH and AZS particles in the glassy phase, responsible of the mechanical properties increase after high-temperatures exposure.

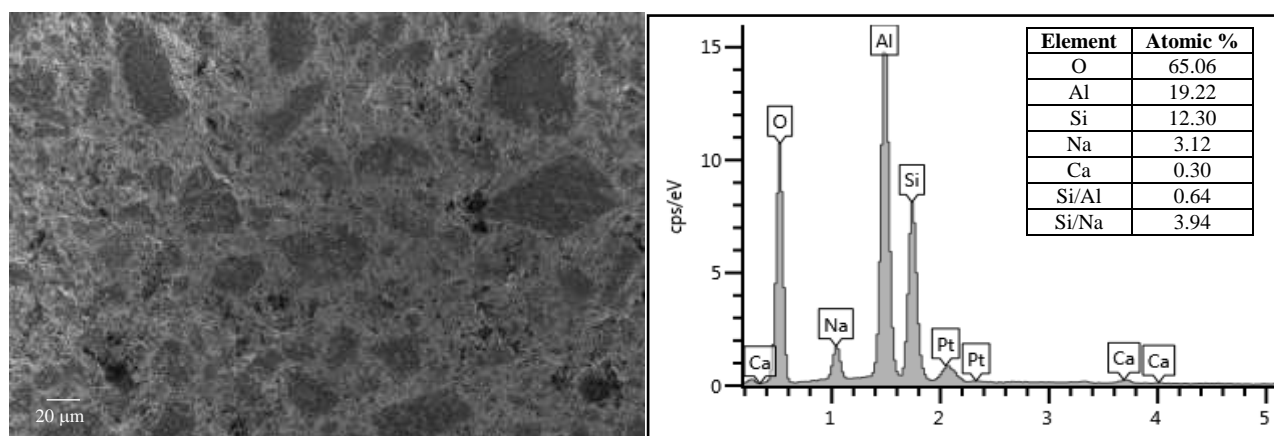


**Figure 18:** FE-SEM micrograph of as-prepared CH paste and EDS semiquantitative analysis (Pt was used for samples metallization)

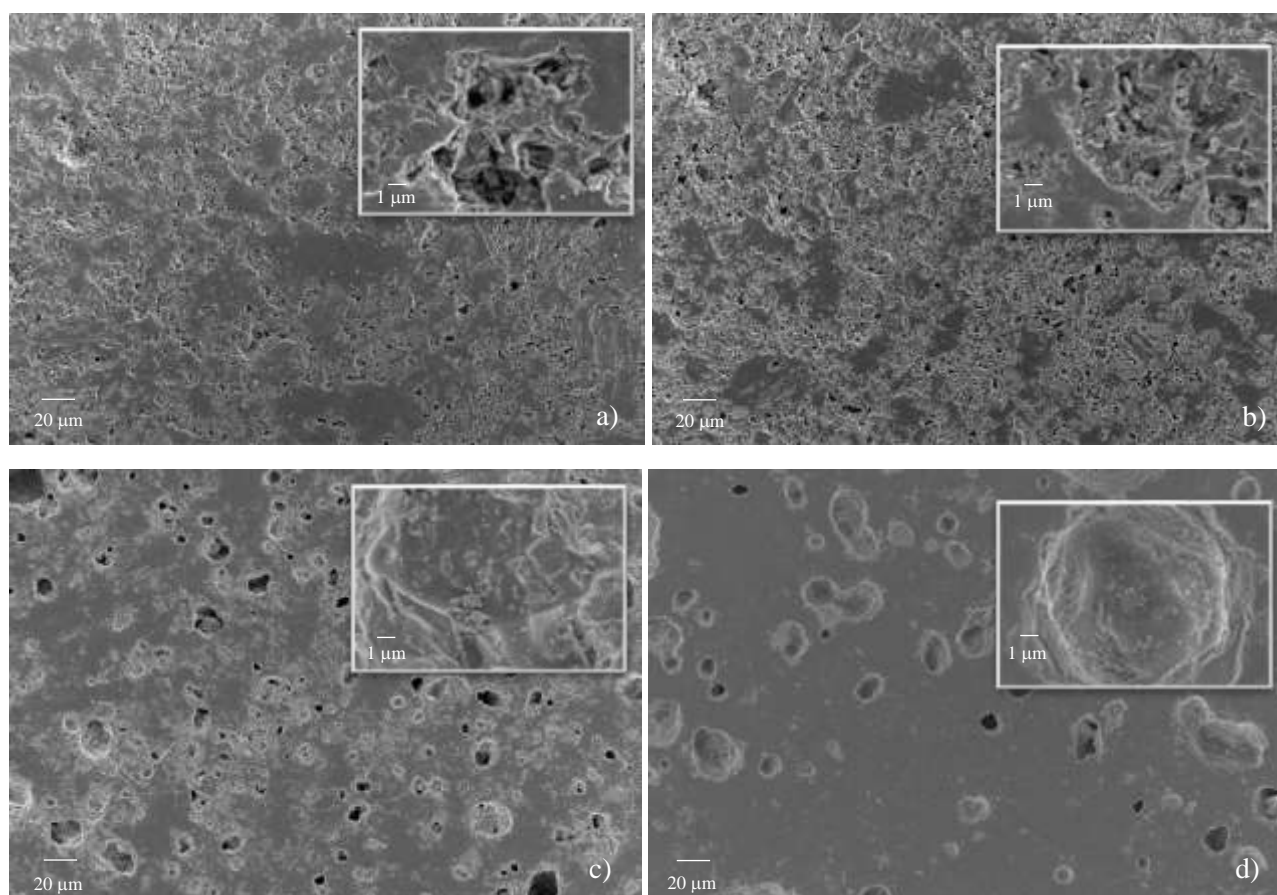


**Figure 19:** FE-SEM micrographs of CH pastes after exposure to: a) 800 °C, b) 1000 °C, c) 1200 °C and d) 1400 °C

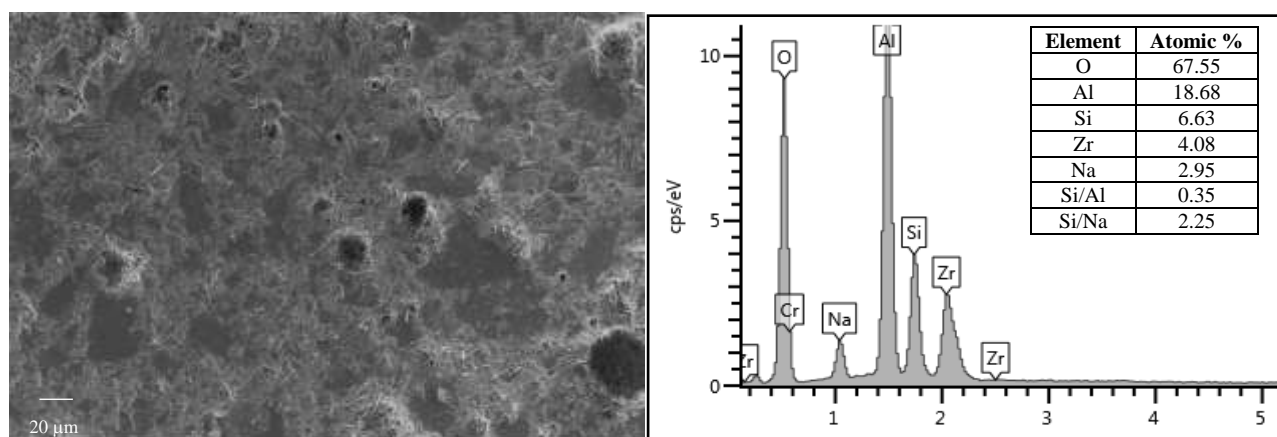


**Figure 20:** FE-SEM micrograph of as-prepared AZS paste and EDS semiquantitative analysis (Cr was used for samples metallization)

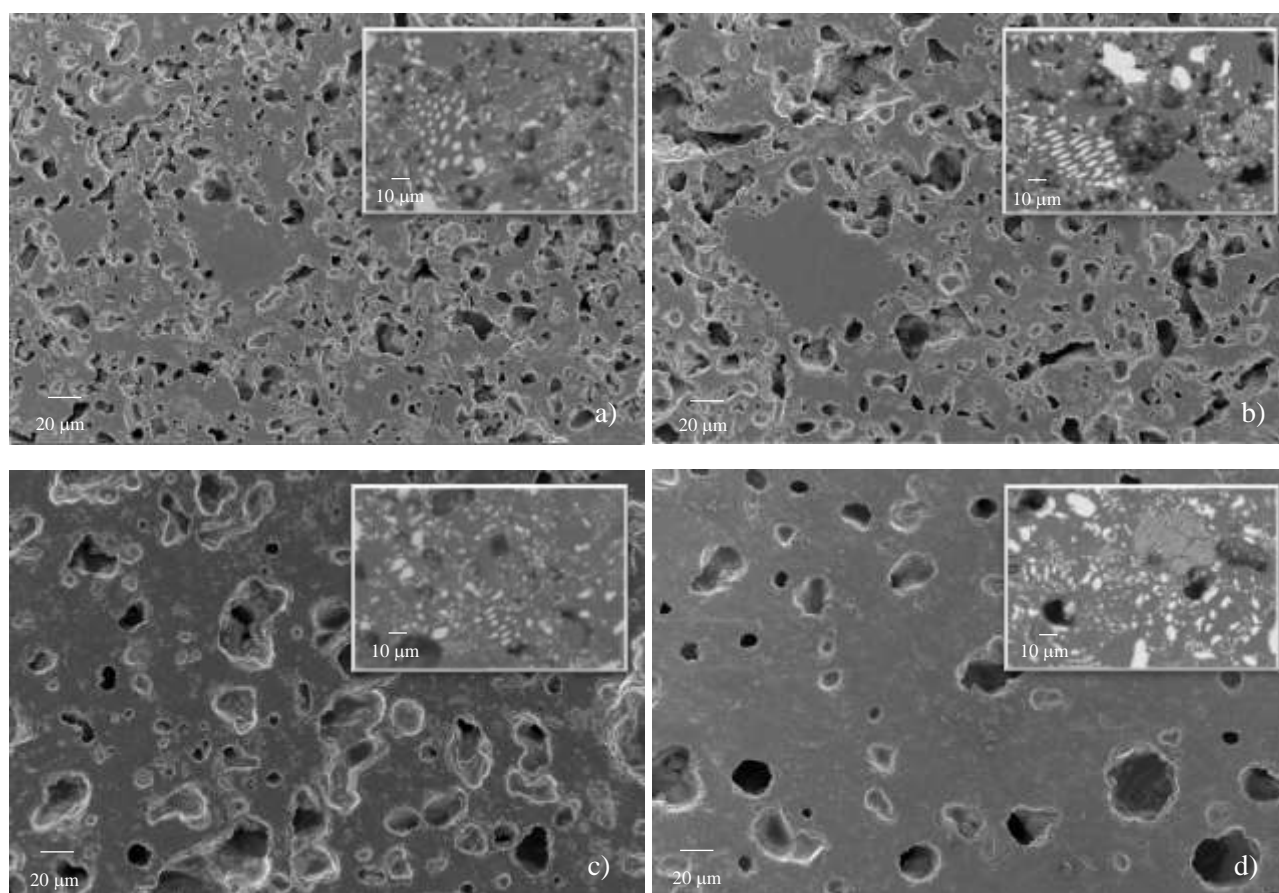


**Figure 21:** FE-SEM micrographs of AZS pastes after exposure to: a) 800 °C, b) 1000 °C, c) 1200 °C and d) 1400 °C

#### 4. Conclusions

Alkali-activated pastes were successfully prepared using two kinds of aluminosilicate refractory wastes as raw materials, and their properties after exposure to high-temperatures (i.e. 800, 1000, 1200 and 1400 °C) were investigated. In particular, waste alumina-zirconia-silica (AZS) and chamotte (CH) powders, milled to achieve a very fine particle size distribution ( $d_{50} \sim 5\text{--}6\text{ }\mu\text{m}$ ), were selected, and mixed with an alkaline aqueous solution of sodium hydroxide and sodium silicate ( $\text{SiO}_2/\text{Na}_2\text{O}$  molar ratio of 1.65), to produce alkali-activated materials (AA-CH and AA-AZS, respectively). XRD and FT-IR demonstrated the occurrence of a certain reactivity between raw powders and alkaline solution, and particularly the formation of zeolitic hydrated phases. Moreover, the very high strength of the developed pastes (compressive strength of 60 and 70 MPa for AA-AZS and AA-CH, respectively) supports the hypothesis of an effective alkaline-activation of the raw powders and the formation of a binding phase well joining the undissolved larger particles. So, this is a strong point of innovation compared to previous literature, where refractory particles

were used in geopolymers as fillers or aggregates, but never as feedstock powder. Even more, the use of AZS in these kinds of materials is very new in literature, while the important fraction glassy silicates contained offers interesting opportunity in the alkali-activation process, besides the refractory properties of the electrical melted alumina and zirconia phases.

A sharp increase of mechanical properties was obtained after exposure of both AA-pastes at high-temperatures. In particular, as regard as flexural strength, it increased of approx. 250% (after firing at 800 and 1000 °C) and 430% (1200 and 1400 °C) for AA-AZS pastes while the increase was of approx. 740, 660, 840 and 750% for AA-CH pastes after firing at 800, 1000, 1200 and 1400 °C, respectively. Then, as regard as compressive strength, it increased of approx. 90% (after firing at 800 and 1000 °C) and 200% (1200 and 1400 °C) for AA-AZS pastes while the increase was of approx. 160% (after firing at 800 and 1000 °C) and 210% (1200 °C) for AA-CH while slightly increased after firing at 1400 °C (40%). Mechanical strength increase after exposure to 800 and 1000 °C can be related to densification of the glassy phase that binds together undissolved particles, as demonstrated by FE-SEM observations, and to the formation of new crystalline phases from the binder gel (albite and nepheline, for CH and AZS-based pastes, respectively), observed in XRD patterns. Moreover, MIP analysis reported a decrease of micro and meso-porosity. A further increase of the firing temperature up to 1200 °C leads to materials sintering and shrinkage, with an important porosity reduction. These phenomena are responsible of a further increase of mechanical properties for both samples that remain constant for AZS samples even after exposure at 1400 °C, while decreased for AA-CH materials, due to andalusite decomposition, and cracks formation in the fired samples. Considering possible applications, a limit to their use is related to dimensional changes when exposed to high temperatures, even if comparable or even lower than those already reported in literature. Anyway, due the exceptional properties achieved, they can be used as matrix materials to produce precast mortars or concretes blocks, by exploiting the same refractories but with larger particles size, in order to reduce as much as possible the matrix-reinforcement thermal expansion mismatch. Therefore, these materials show potential for the construction sector, in fire-protection systems or for the production of new refractories from waste materials. Besides dense specimens, the development of lightweight blocks for high-temperature application will be investigated as well.

## Acknowledgments

The researches leading to these results have received funding from the European project AMITIE (Marie Skłodowska Curie Grant Agreement n°734342). Authors are grateful to Ingessil s.r.l for the sodium silicate solution.

## References

- 1 F. Pacheco-Torgal, J. Castro-Gomes, S. Jalali, Alkali-activated binders: A review: Part 1. Historical background, terminology, reaction mechanisms and hydration products, *Constr. Build. Mater.*, 22 (2008) 1305-1314. <https://doi.org/10.1016/j.conbuildmat.2007.10.015>
- 2 J.L. Provis, Alkali-activated materials, *Cem. Concr. Res.* 114 (2018) 40-48. <https://doi.org/10.1016/j.cemconres.2017.02.009>
- 3 L. Coppola, T. Bellezze, A. Belli, M.C. Bignozzi, F. Bolzoni, A. Brenna, et al., Binders alternative to Portland cement and waste management for sustainable construction—Part 1, *J. Appl. Biomater. Funct. Mater.*, 16 2018 186-202. <https://doi.org/10.1177/2280800018782845>
- 4 Y.M. Amran, R. Alyousef, H. Alabduljabbar, M. El-Zeadani, Clean production and properties of geopolymer concrete; A review, *J. Clean. Prod.*, (2020) 119679. <https://doi.org/10.1016/j.jclepro.2019.119679>
- 5 B. Coppola, P. Palmero, L. Montanaro, J.M. Tulliani, Alkali-activation of marble sludge: influence of curing conditions and waste glass addition, *J. Eur. Ceram. Soc.*, (2019). <https://doi.org/10.1016/j.jeurceramsoc.2019.11.068>
- 6 M. Bassani, L. Tefa, B. Coppola, P. Palmero, Alkali-activation of aggregate fines from construction and demolition waste: Valorisation in view of road pavement subbase applications, *J. Clean. Prod.*, 234 (2019) 71-84. <https://doi.org/10.1016/j.jclepro.2019.06.207>
- 7 P. Palmero, A. Formia, J.M. Tulliani, P. Antonaci, Valorisation of alumino-silicate stone muds: From wastes to source materials for innovative alkali-activated materials, *Cem. Concr. Compos.*, 83 (2017) 251-262. <https://doi.org/10.1016/j.cemconcomp.2017.07.011>
- 8 R.E. Lyon, P.N. Balaguru, A. Foden, U. Sorathia, J. Davidovits, M. Davidovics, Fire-resistant aluminosilicate composites, *Fire Mater.*, 21 (1997) 67-73. [https://doi.org/10.1002/\(SICI\)1099-1018\(199703\)21:2%3C67::AID-FAM596%3E3.0.CO;2-N](https://doi.org/10.1002/(SICI)1099-1018(199703)21:2%3C67::AID-FAM596%3E3.0.CO;2-N)
- 9 J.A. Hammell, P.N. Balaguru, R.E. Lyon, Strength retention of fire resistant aluminosilicate-carbon composites under wet-dry conditions, *Compos. B. Eng.*, 31 (2000) 107-111. [https://doi.org/10.1016/S1359-8368\(99\)00072-4](https://doi.org/10.1016/S1359-8368(99)00072-4)
- 10 M. Hussain, R.J. Varley, Y.B. Cheng, G.P. Simon, Investigation of thermal and fire performance of novel hybrid geopolymer composites, *J. Mater. Sci.*, 39 (2004) 4721-4726. <https://doi.org/10.1023/B:JMSC.0000034180.35216.ba>
- 11 D.C. Comrie, W.M. Kriven, Composite cold ceramic geopolymer in a refractory application. in NP Bansal, JP Singh, WM Kriven & H Schneider (eds), *Advances in Ceramics Matrix Composites IX*, Proceedings, Ceramic Transactions, 153 (2004) 211-225, Nashville, TN, United States.
- 12 D.S. Perera, R.L. Trautman, Geopolymers with the potential for use as refractory castables, *Advances in Technology of Materials and Materials Processing Journal (ATM)*, 7 (2005) 187-190. <https://doi.org/10.2240/azojomo0173>

- 13 V. Vaou, D. Papias, Thermal insulating foamy geopolymers from perlite, *Miner. Eng.*, 23 (2010) 1146-1151. <https://doi.org/10.1016/j.mineng.2010.07.015>
- 14 W.M. Kriven, J. Bell, M. Gordon, Geopolymer Refractories for the Glass Manufacturing Industry, *Ceramic engineering and science proceedings*, 25 (2004) 57-79.
- 15 G. Kovalchuk, P.V. Krienko, Producing fire-and heat-resistant geopolymers, *Geopolymers* (2009) 227-266, Woodhead Publishing. <https://doi.org/10.1533/9781845696382.2.227>
- 16 J. Poirier, P. Prigent, M.L. Bouchetou, The effects of fine and ultra-fine particles on the design of refractory ceramics, *Refract. Worldforum*, 3 [2] (2011) 99-109.
- 17 L. Horekmans, P. Nielsen, P. Dierckx, A. Ducastel, Recycling of refractory bricks used in basic steelmaking: A review, *Resour. Conserv. Recy.*, 140 (2019) 297-304. <https://doi.org/10.1016/j.resconrec.2018.09.025>
- 18 C. Sadik, I.E. El Amrani, A. Albizane, Recent advances in silica-alumina refractory: A review, *J. Asian Ceram. Soc.*, 2 (2014) 83-96. <https://doi.org/10.1016/j.jascers.2014.03.001>
- 19 C. Schacht, *Refractories handbook*, CRC Press, Boca Raton, 2004. <https://www.crcpress.com/Refractories-Handbook/Schacht/p/book/9780824756543>
- 20 K. Dana, S. Sinhamahapatra, H.S. Tripathi, A. Ghosh, Refractories of Alumina-Silica System, *T. Indian. Ceram. Soc.*, 73 (2014) 1-13. <https://doi.org/10.1080/0371750X.2014.905265>
- 21 G.V. Carbajal, J.R. Galicia, J.R. Ángeles, J.L. Cuevas, C.G. Chavarría, Microstructure and mechanical behavior of alumina–zirconia–mullite refractory materials, *Ceram. Int.*, 38 (2012) 1617-1625. <https://doi.org/10.1016/j.ceramint.2011.09.051>
- 22 L.J. Manfredo, R.N. McNally, The corrosion resistance of high ZrO<sub>2</sub> fusion-cast Al<sub>2</sub>O<sub>3</sub>-ZrO<sub>2</sub>-SiO<sub>2</sub> glass refractories in soda lime glass, *J. Mater. Sci.*, 19 (1984) 1272-1276. <https://doi.org/10.1007/BF01120038>
- 23 A.M. Guzmán, D.I. Martínez, R. González, Corrosion–erosion wear of refractory bricks in glass furnaces, *Eng. Fail. Anal.*, 46 (2014) 188-195. <https://doi.org/10.1016/j.engfailanal.2014.09.003>
- 24 V. Gottardi, Refractories for the glass industry, *J. Non-Cryst. Solids*, 80 (1986) 93-102. [https://doi.org/10.1016/0022-3093\(86\)90382-0](https://doi.org/10.1016/0022-3093(86)90382-0)
- 25 A. Moosavi, S. Asadi, H.J. Shoraki, Microstructure and mechanical properties of tabular alumina composites with geopolymer binder at elevated temperatures, *Ceram. Int.*, 45 (2019) 9092-9098. <https://doi.org/10.1016/j.ceramint.2019.01.246>
- 26 K. Hemra, P. Aungkavattana, Effect of cordierite addition on compressive strength and thermal stability of metakaolin based geopolymer, *Adv. Powder. Technol.*, 27 (2016) 1021-1026. <https://doi.org/10.1016/j.appt.2016.04.019>
- 27 L. Carabba, S. Manzi, E. Rambaldi, G. Ridolfi, M.C. Bignozzi, High-temperature behaviour of alkali-activated composites based on fly ash and recycled refractory particles, *J. Ceram. Sci. Technol.*, 8 (2017) 377-388. <https://doi.org/10.4416/JCST2017-00047>
- 28 S.S. Musil, W.M. Kriven, In situ mechanical properties of chamotte particulate reinforced, potassium geopolymer, *J. Am. Ceram. Soc.*, 97 (2014) 907-915. <https://doi.org/10.1111/jace.12736>
- 29 S.A. Bernal, J. Bejarano, C. Garzón, R.M. de Gutiérrez, S. Delvasto, E.D. Rodríguez, Performance of refractory aluminosilicate particle/fiber-reinforced geopolymer composites, *Compos. B. Eng.*, 43 (2012) 1919-1928. <https://doi.org/10.1016/j.compositesb.2012.02.027>

- 30 T. Kovářik, L. Kullová, D. Rieger, Production of refractory chamotte particle-reinforced geopolymer composite. In IOP Conference Series: Materials Science and Engineering, 123 (2016) 012041. IOP Publishing. <https://doi.org/10.1088/1757-899X/123/1/012041>
- 31 T. Kovářik, D. Rieger, J. Kadlec, T. Křenek, L. Kullová, M. Pola, P. Bělský, P. Franče, J. Říha, Thermomechanical properties of particle-reinforced geopolymer composite with various aggregate gradation of fine ceramic filler, Constr. Build. Mater., 143 (2017) 599-606. <https://doi.org/10.1016/j.conbuildmat.2017.03.134>
- 32 A.C. Trindade, F.D. Silva, H.A. Alcamand, P.H. Borges, On The Mechanical Behavior of Metakaolin Based Geopolymers Under Elevated Temperatures, Mater. Res., 20 (2017) 265-72. <http://dx.doi.org/10.1590/1980-5373-mr-2017-0101>
- 33 C.N. Djangang, C. Tealdi, A.S. Cattaneo, P. Mustarelli, E. Kamseu, C. Leonelli, Cold-setting refractory composites from cordierite and mullite–cordierite design with geopolymer paste as binder: Thermal behavior and phase evolution, Mater. Chem. Phys., 154 (2015) 66-77. <https://doi.org/10.1016/j.matchemphys.2015.01.046>
- 34 P. Rovnaník, K. Šafránková, Thermal behaviour of metakaolin/fly ash geopolymers with chamotte aggregate, Materials, 9 (2016) 535. <https://doi.org/10.3390/ma9070535>
- 35 S. Wattanasiriwech, F.A. Nargesang, D. Wattanasiriwech, P. Timakul, Characterisation and properties of geopolymer composite part 1: Role of mullite reinforcement, Ceram. Int., 43 (2017) 16055-16062. <https://doi.org/10.1016/j.ceramint.2017.06.166>
- 36 S. Wattanasiriwech, F.A. Nargesang, D. Wattanasiriwech, P. Timakul, Characterisation and properties of geopolymer composites. Part 2: Role of cordierite-mullite reinforcement, Ceram. Int., 43 (2017) 16063-16069. <https://doi.org/10.1016/j.ceramint.2017.08.215>
- 37 O.G. Rivera, W.R. Long, C.A. Weiss Jr, R.D. Moser, B.A. Williams, K. Torres-Cancel, E.R. Gore, P.G. Allison, Effect of elevated temperature on alkali-activated geopolymeric binders compared to portland cement-based binders, Cem. Concr. Res., 90 (2016) 43-51. <https://doi.org/10.1016/j.cemconres.2016.09.013>
- 38 D.L. Kong, J.G. Sanjayan, Effect of elevated temperatures on geopolymer paste, mortar and concrete, Cem. Concr. Res., 40 (2010) 334-339. <https://doi.org/10.1016/j.cemconres.2009.10.017>
- 39 C. Kuenzel, L.M. Grover, L. Vandeperre, A.R. Boccaccini, C.R. Cheeseman, Production of nepheline/quartz ceramics from geopolymer mortars, J. Eur. Ceram. Soc., 33 (2013) 251-258. <https://doi.org/10.1016/j.jeurceramsoc.2012.08.022>
- 40 C.K. Yip, J.L. Provis, G.C. Lukey, J.S. van Deventer, Carbonate mineral addition to metakaolin-based geopolymers, Cem. Concr. Compos., 30 (2008) 979-985. <https://doi.org/10.1016/j.cemconcomp.2008.07.004>
- 41 L. Zuda, P. Bayer, P. Rovnaník, R. Černý, Mechanical and hydric properties of alkali-activated aluminosilicate composite with electrical porcelain aggregates, Cem. Concr. Compos., 30 (2008) 266-273. <https://doi.org/10.1016/j.cemconcomp.2007.11.003>
- 42 S.A. Bernal, E.D. Rodríguez, R. Mejía de Gutiérrez, J.L. Provis, Performance at high temperature of alkali-activated slag pastes produced with silica fume and rice husk ash based activators, Mater. Construcc., 65 (2015). <http://dx.doi.org/10.3989/mc.2015.03114>
- 43 A.M. Rashad, D.M. Sadek, H.A. Hassan, An investigation on blast-furnace slag as fine aggregate in alkali-activated slag mortars subjected to elevated temperatures, J. Clean. Prod., 112 (2016) 1086-96. <https://doi.org/10.1016/j.jclepro.2015.07.127>
- 44 B. Coppola, L. Di Maio, P. Scarfato, L. Incarnato, Use of polypropylene fibers coated with nano-silica particles into a cementitious mortar. In AIP Conference Proceedings, 1695 (2015) 020056, AIP Publishing. <https://doi.org/10.1063/1.4937334>



- 45 G. Ferrara, B. Coppola, L. Di Maio, L. Incarnato, E. Martinelli, Tensile strength of flax fabrics to be used as reinforcement in cement-based composites: experimental tests under different environmental exposures, *Compos. B. Eng.*, 168 (2019) 511-523. <https://doi.org/10.1016/j.compositesb.2019.03.062>
- 46 J. Yuan, P. He, D. Jia, S. Yan, D. Cai, L. Xu, Z. Yang, X. Duan, S. Wang, Y. Zhou, SiC fiber reinforced geopolymer composites, part 1: Short SiC fiber, *Ceram. Int.*, 42 (2016) 5345-5352. <https://doi.org/10.1016/j.ceramint.2015.12.067>
- 47 P. Timakul, W. Rattanaprasit, P. Aungkavattana, Improving compressive strength of fly ash-based geopolymer composites by basalt fibers addition, *Ceram. Int.*, 42 (2016) 6288-6295. <https://doi.org/10.1016/j.ceramint.2016.01.014>
- 48 R. Heidrich, A. Gupta, Fused cast AZS glassy phase exudation: Intrinsic or pathological property? *RHI Bulletin*, 2 (2011) 24-28.
- 49 A. Tomba, M.A. Camerucci, G. Urretavizcaya, A.L. Cavalieri, M.A. Sainz, A. Caballero, Elongated mullite crystals obtained from high temperature transformation of sillimanite, *Ceram. Int.*, 25 (1999) 245-252. [https://doi.org/10.1016/S0272-8842\(98\)00031-5](https://doi.org/10.1016/S0272-8842(98)00031-5)
- 50 L.A. Johnson, R.A. McCauley, The thermal behavior of albite as observed by DTA, *Thermochim. Acta*, 437 (2005) 134-139. <https://doi.org/10.1016/j.tca.2005.06.039>
- 51 T.J. Tenner, R.A. Lange, R.T. Downs, The albite fusion curve re-examined: New experiments and the high-pressure density and compressibility of high albite and NaAlSi<sub>3</sub>O<sub>8</sub> liquid, *Am. Mineral.*, 92 (2007) 1573-1585. <https://doi.org/10.2138/am.2007.2464>
- 52 J.G. Liou, Alcalcime equilibria, *Lithos*, 4 (1971) 389-402. [http://doi.org/10.1016/0024-4937\(71\)90122-8](http://doi.org/10.1016/0024-4937(71)90122-8)
- 53 D.R. Johnson, N.B. Young, W.A. Robb, Thermal characteristics of analcime and its effect on heat requirements for oil-shale retorting, *Fuel*, 54 (1975) 249-252. [https://doi.org/10.1016/0016-2361\(75\)90038-1](https://doi.org/10.1016/0016-2361(75)90038-1)
- 54 C.J. Peng, Thermal analysis study of the natrolite group, *Am. Mineral.*, 40 (1955) 834-856.
- 55 L.P. van Reeuwijk, The thermal dehydration of natural zeolites (Doctoral dissertation, Veenman), 1974.
- 56 T. Bakharev, Thermal behaviour of geopolymers prepared using class F fly ash and elevated temperature curing, *Cem. Concr. Res.*, 36 (2006) 1134-1147. <https://doi.org/10.1016/j.cemconres.2006.03.022>
- 57 M.X. Peng, Z.H. Wang, Q.G. Xiao, F. Song, W. Xie, L.C. Yu, H.W. Huang, S.J. Yi, Effects of alkali on one-part alkali-activated cement synthesized by calcining bentonite with dolomite and Na<sub>2</sub>CO<sub>3</sub>, *Appl. Clay Sci.*, 139 (2017) 64-71. <https://doi.org/10.1016/j.clay.2017.01.020>
- 58 G. Zhang, Z. Li, L. Zhang, Y. Shang, H. Wang, Experimental research on drying control condition with minimal effect on concrete strength, *Constr. Build. Mater.*, 135 (2017) 194-202. <https://doi.org/10.1016/j.conbuildmat.2016.12.141>
- 59 B. Li, M. He, H. Wang, Phase transformation of andalusite-mullite and its roles in the microstructure and sinterability of refractory ceramic, *Metall. Mater. Trans. A*, 48 (2017) 3188-3192. <https://doi.org/10.1007/s11661-017-4092-z>
- 60 C. Wang, M. Zinkevich, F. Aldinger, The zirconia-hafnia system: DTA measurements and thermodynamic calculations, *J. Am. Ceram. Soc.*, 89 (2006) 3751-3758. <https://doi.org/10.1111/j.1551-2916.2006.01286.x>
- 61 P. Rovnaník, P. Bayer, P. Rovnaníková, Characterization of alkali activated slag paste after exposure to high temperatures, *Constr. Build. Mater.*, 47 (2013) 1479-1487. <https://doi.org/10.1016/j.conbuildmat.2013.06.070>



- 62 M. Mohabbi Yadollahi, M. Dener, Investigation of elevated temperature on compressive strength and microstructure of alkali activated slag based cements, *Eur. J. Environ. Civ. En.*, (2019) 1-5.  
<https://doi.org/10.1080/19648189.2018.1557562>
- 63 M. Okuno, N. Zotov, M. Schmücker, H. Schneider, Structure of  $\text{SiO}_2\text{--Al}_2\text{O}_3$  glasses: combined X-ray diffraction, IR and Raman studies, *J. Non-Cryst. Solids*, 351 (2005) 1032-1038.  
<https://doi.org/10.1016/j.jnoncrysol.2005.01.014>
- 64 P. Padmaja, G.M. Anilkumar, P. Mukundan, G. Aruldas, K.G.K. Warriar, Characterisation of stoichiometric sol–gel mullite by fourier transform infrared spectroscopy, *Int. J. Inorg. Mater.*, 3 (2001) 693-698. [https://doi.org/10.1016/S1466-6049\(01\)00189-1](https://doi.org/10.1016/S1466-6049(01)00189-1)
- 65 P. Duxson, G.C. Lukey, J.S. van Deventer, Physical evolution of Na-geopolymer derived from metakaolin up to 1000 °C, *J. Mater. Sci.*, 42 (2007) 3044-3054. <https://doi.org/10.1007/s10853-006-0535-4>
- 66 E.Y. Fogaing, M. Huger, C. Gault, Elastic properties and microstructure: study of two fused cast refractory materials, *J. Eur. Ceram. Soc.*, 27 (2007) 1843-1848.  
<https://doi.org/10.1016/j.jeurceramsoc.2006.04.149>
- 67 A.M. Rashad, S.R. Zeedan, A.A. Hassan, Influence of the activator concentration of sodium silicate on the thermal properties of alkali-activated slag pastes, *Constr. Build. Mater.*, 102 (2016) 811-20.  
<https://doi.org/10.1016/j.conbuildmat.2015.11.023>
- 68 C. Giosuè, A. Mobili, C. Di Perna, F. Tittarelli, Performance of lightweight cement-based and alkali-activated mortars exposed to high-temperature, *Constr. Build. Mater.*, 220 (2019) 565-576.  
<https://doi.org/10.1016/j.conbuildmat.2019.05.193>
- 69 W.D. Rickard, C.S. Kealley, A. Van Riessen, Thermally induced microstructural changes in fly ash geopolymers: experimental results and proposed model, *J. Am. Ceram. Soc.*, 98 (2015) 929-939.  
<https://doi.org/10.1111/jace.13370>
- 70 J. Li, Y. Pan, C. Xiang, Q. Ge, J. Guo, Low temperature synthesis of ultrafine  $\alpha\text{-Al}_2\text{O}_3$  powder by a simple aqueous sol–gel process, *Ceram. Int.*, 32 (2006) 587-591.  
<https://doi.org/10.1016/j.ceramint.2005.04.015>
- 71 H.R. Sahu, G.R. Rao, Characterization of combustion synthesized zirconia powder by UV-vis, IR and other techniques, *Bull. Mater. Sci.*, 23 (2000) 349-354. <https://doi.org/10.1007/BF02708383>
- 72 M. Tomozawa, M. Takata, J. Acocella, E.B. Watson, T. Takamori, Thermal properties of  $\text{Na}_2\text{O} \cdot 3\text{SiO}_2$  glasses with high water content, *J. Non-Cryst. Solids*, 56 (1983) 343-348. [https://doi.org/10.1016/0022-3093\(83\)90491-X](https://doi.org/10.1016/0022-3093(83)90491-X)
- 73 E.V. Belova, Y.A. Kolyagin, I.A. Uspenskaya, Structure and glass transition temperature of sodium-silicate glasses doped with iron, *J. Non-Cryst. Solids*, 423 (2015), 50-57.  
<https://doi.org/10.1016/j.jnoncrysol.2015.04.039>